

1 We thank the editor for the thoughtful comments. We address each comment individually  
2 below, with the editor's initial comment in **black** and our responses in **blue**.

### 3 **Response to the editor**

4 In the abstract, I would like you to endeavour to be very explicit in distinguishing clusters of mass  
5 spectra versus clusters of molecules forming aerosol. I leave it to you to find the best language,  
6 but suggest 'clusters of spectra' and 'aerosol particles' are used throughout the abstract, for  
7 clarity. I realise this may seem heavy-handed, but I'm concerned especially for inexperienced  
8 researchers whose first language may not be English.

9

10 We have added "mass spectral" to describe clusters.

11

12 Line 86, please delete "a new clustering method" and change 'a novel extension' to 'an extension'.

13 Line 116: please delete 'novel'

14 Line 312: please delete 'if any' (I think the meaning is already captured in the parentheses  
15 immediately beforehand).

16

17 We have deleted the words accordingly.

18

19 At the end of section 2.2, I would welcome a paragraph summarising the truly automated process  
20 and the part requiring human input (and when this input is for every experiment or just for every  
21 new kind of experiment). Please could you think about how you might convey an estimate of the  
22 time saved? Or is it not so much time saved as patterns found objectively? If that is the case,  
23 please say so.

24

25 We have added a paragraph as section 2.2.4 to summarize the algorithm.

26

27 Line 407ff. I think more is needed here about why it is better to look only at neighbours of the  
28 seed, rather than neighbours of the neighbours. Can elaborate your argument that NSSC is a  
29 development of DBScan and make sure it does not appear to be a simplification requiring quite  
30 a lot of data pre- and post-processing?

31

32 We have added several sentences in section 2.3 to address the concern.

33

34

35 **A robust clustering algorithm for analysis of composition-dependent**  
36 **organic aerosol thermal desorption measurements**

37 Ziyue Li<sup>1</sup>, Emma L. D'Ambro<sup>2,3,a</sup>, Siegfried Schobesberger<sup>2,4</sup>, Cassandra J. Gaston<sup>2,b</sup>, Felipe D.  
38 Lopez-Hilfiker<sup>2,c</sup>, Jiumeng Liu<sup>5,d</sup>, John E. Shilling<sup>5</sup>, Joel A. Thornton<sup>2,3</sup>, Christopher D. Cappa<sup>1,6</sup>

39 <sup>1</sup> Atmospheric Science Graduate Group, University of California, Davis, CA, USA

40 <sup>2</sup> Department of Atmospheric Sciences, University of Washington, Seattle WA, USA

41 <sup>3</sup> Department of Chemistry, University of Washington, Seattle WA, USA

42 <sup>4</sup> Department of Applied Physics, University of Eastern Finland, Kuopio, Finland

43 <sup>5</sup> Atmospheric Sciences and Global Change Division, Pacific Northwest National Laboratory,  
44 Richland WA, USA

45 <sup>6</sup> Department of Civil and Environmental Engineering, University of California, Davis, CA, USA

46 <sup>a</sup> Oak Ridge Institute for Science and Education, US Environmental Protection Agency, Research  
47 Triangle Park, NC, USA

48 <sup>b</sup> Rosenstiel School of Marine & Atmospheric Science, University of Miami FL, USA

49 <sup>c</sup> TofWerk AG, Thun, Switzerland

50 <sup>d</sup> Now at: School of Environment, Harbin Institute of Technology, Harbin, Heilongjiang, China

51 **Abstract**

52 One of the challenges of understanding atmospheric organic aerosol (OA) particles stems from  
53 its complex composition. Mass spectrometry is commonly used to characterize the compositional  
54 variability of OA. Clustering of a mass spectral data set helps identify components that exhibit  
55 similar behavior or have similar properties, facilitating understanding of sources and processes  
56 that govern compositional variability. Here, we developed an algorithm for clustering mass  
57 spectra, Noise-Sorted Scanning Clustering (NSSC), appropriate for application to thermal  
58 desorption measurements of collected OA particles from the Filter Inlet for Gases and AEROSols  
59 coupled to a chemical ionization mass spectrometer (FIGAERO-CIMS). NSSC, which extends the  
60 common DBSCAN algorithm, provides a robust, reproducible analysis of the FIGAERO  
61 temperature-dependent mass spectral data. The NSSC allows for determination of thermal  
62 profiles for compositionally distinct clusters of mass spectra, increasing the accessibility and  
63 enhancing the interpretation of FIGAERO data. Applications of NSSC to several laboratory  
64 biogenic secondary organic aerosol (BSOA) systems demonstrate the ability of NSSC to  
65 distinguish different types of thermal behaviors for the components comprising the particles  
66 along with the relative mass contributions and chemical properties (e.g. average molecular  
67 formula) of each mass spectral cluster. For each of the systems examined, more than 80% of the  
68 total mass is clustered into 9-13 mass spectral clusters. Comparison of the average thermograms  
69 of the mass spectral clusters between systems indicate some commonality in terms of the thermal  
70 properties of different BSOA, although with some system-specific behavior. Application of NSSC  
71 to sets of experiments in which one experimental parameter, such as the concentration of NO, is  
72 varied demonstrates the potential for mass spectral clustering to elucidate the chemical factors  
73 that drive changes in the thermal properties of OA particles. Further quantitative interpretation

Deleted: clustering

75 of the thermograms of the mass spectral clusters will allow for more comprehensive  
76 understanding of the thermochemical properties of OA particles.

Deleted: clustered

Deleted: followed by clustering

## 77 1. Introduction

78 Atmospheric particles are composed of hundreds to thousands of individual compounds  
79 (e.g., Hamilton et al., 2004; Goldstein and Galbally, 2007), reflecting the many different sources  
80 and the variety of chemical pathways that lead to their formation and growth. Various mass  
81 spectrometry (MS) methods provide for characterization of this compositional variability, among  
82 other techniques. Individual MS methods yield different insights into particle composition,  
83 dependent upon the chemical selectivity of the method. Application of various data reduction  
84 methods, such as clustering or matrix factorization, helps to reduce the inherent compositional  
85 complexity and develop understanding of the sources and chemical transformations that  
86 determine particle composition. Clustering and matrix factorization are complementary methods.  
87 In this work, we develop and apply a new clustering method to measurements of the evolved gas  
88 composition derived from thermal desorption of organic aerosol, specifically to mass spectral  
89 measurements from the Filter Inlet for Gases and AEROsols (Lopez-Hilfiker et al., 2014) coupled  
90 with chemical ionization mass spectrometry (Lee et al., 2014) (FIGAERO-CIMS). The mass spectral  
91 clustering method developed here facilitates interpretation of variability in organic aerosol  
92 composition and volatility, and how these depend on formation conditions.

93 Clustering methods applied across many research fields have aided in the interpretation  
94 and understanding of large data sets. Clustering methods work by classifying data into several  
95 groups according to the similarity between one or more properties. In the field of atmospheric  
96 chemistry, clustering methods have been applied to a variety of data types. Examples include:  
97 back trajectories of trace gases (Cape et al., 2000) or particles (Abdalmogith and Harrison, 2005;  
98 Pinero-Garcia et al., 2015), helping to elucidate the origin and transport of pollutants; particle  
99 size distributions, providing information on aerosol emission and formation (Beddows et al., 2009;  
100 Wegner et al., 2012); and, the morphology of and organic functional groups comprising individual  
101 particles, allowing for classification of the types of organic carbon (Takahama et al., 2007).

102 Beyond the above examples, clustering methods have been extensively applied to the  
103 interpretation of single particle mass spectra, serving to characterize variability in their chemical

106 composition and identify the sources and extent of chemical processing (e.g., Gaston et al., 2013;  
107 Lee et al., 2015). While clustering is a general method, a variety of specific algorithms have been  
108 developed for application to a given particle mass spectral dataset. The algorithms applied to  
109 analysis of single particle mass spectra include: *K*-means (Giorio et al., 2012; Liu et al., 2013; Lee  
110 et al., 2015); fuzzy *c*-means (Kirchner et al., 2003; Roth et al., 2016); density-based special  
111 clustering of applications with noise (DBSCAN) (Zhou et al., 2006); neural network-based  
112 methods, such as an algorithm derived from Adaptive Resonance Theory (ART-2a) (Song et al.,  
113 1999; Zhao et al., 2008; Giorio et al., 2012); hierarchical clustering (Murphy et al., 2003; Rebotier  
114 and Prather, 2007); and, some combined algorithms (Zhao et al., 2008; Reitz et al., 2016). Each  
115 clustering algorithm has strengths and weaknesses. In some cases, different algorithms are  
116 equally effective and lead to similar categorization of the same data set, while in other cases  
117 quite different results are obtained (Zhao et al., 2008). For example, *K*-means and ART-2a gave  
118 broadly similar results on a regional particle data set (Giorio et al., 2012), and *K*-means performed  
119 as well as a variant of hierarchical clustering method on four particle data sets (Rebotier and  
120 Prather, 2007).

121 Here, we describe and apply a clustering method, an extension of DBSCAN appropriate for  
122 analysis of combined thermal desorption-mass spectral measurements of organic particle  
123 composition, specifically applied to data from the FIGAERO-CIMS. FIGAERO-CIMS has been  
124 increasingly used in field (e.g. Gaston et al., 2016; Lee et al., 2016; Lopez-Hilfiker et al., 2016;  
125 Mohr et al., 2017; Huang et al., 2018; Le Breton et al., 2019) and laboratory studies (e.g. Lopez-  
126 Hilfiker et al., 2015; D'Ambro et al., 2017; Wang and Ruiz, 2018) to develop understanding of the  
127 molecular composition of organic aerosols. A key feature of FIGAERO-CIMS is the ability to  
128 characterize the thermal behavior of organic compounds in particles on a near molecular level  
129 (Lopez-Hilfiker et al., 2014). The use of chemical ionization, a relatively soft ionization method,  
130 facilitates detection and characterization of both monomeric and oligomeric parent compounds  
131 in organic aerosols. In FIGAERO-CIMS, particles are collected and then thermally desorbed, with  
132 mass spectra of the evolved gases measured as a function of temperature. This can also be  
133 displayed as a thermogram: the concentration of an ion or sum of ions as a function of desorption  
134 temperature. The temperature at which a thermogram reaches maximum signal, or  $T_{max}$ , provide

Deleted: new

Deleted: novel

137 information on the volatility, while particularly broad desorption shapes can indicate thermal  
138 decomposition, suggesting the presence of lower volatility, possibly oligomeric, material (Lopez-  
139 Hilfiker et al., 2014). A typical FIGAERO-CIMS mass spectrum of either ambient or  
140 laboratory-generated organic aerosol consists of hundreds of individual ions and thermograms,  
141 (D'Ambro et al., 2018; Lee et al., 2018).

142 Previous studies using FIGAERO-CIMS provided insights into particle composition, including  
143 the presence of lower volatility material, based on analysis of the thermograms of several major  
144 ions (Lopez-Hilfiker et al., 2014; D'Ambro et al., 2017; D'Ambro et al., 2018; Lee et al., 2018). We  
145 expand on this previous work through the application of cluster analysis to FIGAERO-CIMS  
146 thermograms. Clustering of FIGAERO-CIMS data provides a means to expand the understanding  
147 developed from single-ion thermograms and establish the contributions of different types of  
148 thermograms to the bulk particles. One previous study clustered FIGAERO-CIMS data using the  
149 K-means algorithm using two parameters: the ion molecular weight and the maximum  
150 desorption temperature (Faxon et al., 2018). What distinguishes our work is that we cluster the  
151 thermogram across the entire desorption period for each ion, with ions grouped according to the  
152 similarity of their overall volatility distribution. We have considered the performance of various  
153 clustering algorithms (including K-means), ultimately concluding that a variant of the DBSCAN  
154 algorithm, which we develop here and name noise-sorted scanning clustering (NSSC), provides  
155 robust performance and has several advantages over other existing algorithms for FIGAERO-CIMS  
156 data. The NSSC algorithm is applied to several laboratory data sets of secondary organic aerosol  
157 (SOA) formed from various precursors and under various conditions, some are previously  
158 described (D'Ambro et al., 2018). In this work we do not aim to provide comprehensive  
159 interpretation of the resulting clustered thermograms in terms of their thermo-chemical  
160 properties (Schobesberger et al., 2018), only to illustrate the potential of clustering to enhance  
161 interpretation of FIGAERO-CIMS and other similar data.

## 162 2. Clustering Method Description

163 Application of a given clustering algorithm to a particular data type involves a number of  
164 steps. Below, we discuss the specific steps for clustering of FIGAERO-CIMS data, including a

Deleted: novel

166 description of our noise-sorted scanning clustering algorithm. A brief discussion of other  
167 algorithms is also provided.

## 168 **2.1. Data Preprocessing**

### 169 **2.1.1. Exclusion of anomalous thermograms**

170 The quality of the data set should be examined prior to clustering. A typical thermogram  
171 exhibits a continuous evolution to a peak, peaking during a temperature ramping period, after  
172 which there is a steady decrease in signal-to-background over time during a constant-  
173 temperature soaking period; the background-corrected signal at all temperatures remains above  
174 zero or around zero within the uncertainties. See section 3.1 for further details of the FIGAERO-  
175 CIMS. An anomalous thermogram, however, contains negative signal with large magnitude.

176 Anomalous thermograms should be excluded from the clustering to assure the quality of  
177 the results, although most such thermograms do not end up clustered with other ions.  
178 Anomalous thermograms are identified as follows. (i) Estimate a reference noise level ( $\sigma_{\text{ref}}$ ) for  
179 each thermogram as the standard deviation of the last 100 points (corresponding to 500 seconds)  
180 of the thermogram at the end of the constant-temperature soaking period, during which the  
181 signals are usually relatively constant. Use of more points incorporates times when the signals  
182 were still decreasing, while use of fewer points provides a less robust estimate of the noise level.  
183 (ii) Find the minimum in the thermogram and calculate the average of this and the 50 points  
184 (corresponding to 250 seconds, or 100 points) before and after the minimum,  $A_{\text{min}}$ . This provides  
185 for consistency with the determination of  $\sigma_{\text{ref}}$  (iii) Identify thermograms for which  $A_{\text{min}} < -3 * |\sigma_{\text{ref}}|$   
186 as anomalous and exclude these associated ions from further analysis. In other words, when a  
187 thermogram has a valley with averaged negative values exceeding the magnitude of three times  
188 of the reference noise level, then it is considered anomalous. The specific criteria specified above  
189 were determined based on consideration of thermograms from 10 distinct SOA experiments.  
190 While these criteria should be robustly applicable to other FIGAERO-CIMS datasets, they can be  
191 adjusted depending on the specific application, data quality, and needs.

192 Ideally, when anomalous ions are identified the original data would be inspected to identify  
193 the likely origin of the anomalous behavior. Possible origins include problems with background

194 subtraction when the blank has substantially higher signal levels than the particle samples, which  
195 can happen when there is residual contamination or incomplete separation of ions having the  
196 same nominal mass. It is also possible that the components detected for the same ion are  
197 different for the particle and blank measurements. In the example systems considered here, we  
198 identified up to five anomalous ions out of what is typically a few hundred total ions.

199 In some cases, it is desirable to compare thermograms between related experiments, for  
200 example the experiments discussed here that investigated the influence of NO concentration on  
201 SOA formation (Section 4.3) and the impact of isothermal dilution on SOA composition and  
202 volatility (Section 4.4). In such cases, ions identified as anomalous for one experiment are  
203 excluded from analysis for all related experiments to ensure consistency.

#### 204 **2.1.2. Euclidean Distance**

205 Any clustering algorithm requires a metric to determine the similarity between two  
206 members in the data set. Here, we use the commonly used Euclidean Distance (ED) as the metric.  
207 A smaller *ED* indicates greater similarity. A FIGAERO thermogram has *n* points, with all  
208 thermograms having an equal number of points in a data set. A data set here is defined as the  
209 collection of thermograms for all individual ions measured for a single desorption event. The *ED*  
210 between two thermograms *a* and *b* is calculated as:

211

$$212 \quad ED_{a,b} = \sum_n \sqrt{(a_n - b_n)^2} \quad (1)$$

213

214 An individual *ED* value is obtained for every pair of ions in the mass spectrum, resulting in an *n* x  
215 *n* matrix of *ED* values with the diagonal elements all zero. The signal levels between individual  
216 ions differ substantially, reflecting their relative abundances. Therefore, the *ED* calculation uses  
217 normalized thermograms, allowing for comparison between thermogram profiles irrespective of  
218 signal magnitude. Normalization is achieved by dividing each point of the original thermogram  
219 by the thermogram maximum, where the maximum is determined after smoothing using a  
220 35-point boxcar moving average with the end points excluded from the smoothed thermogram.  
221 Use of the smoothed maximum instead of the unsmoothed maximum reduces the influence of

222 noise on normalization. In the FIGAERO datasets used in this study, a typical thermogram has a  
223 temperature resolution of  $\Delta T \sim 0.7$  °C during the ramping period, and a 35-point smooth  
224 corresponds to smoothing over  $\sim 24.5$  °C. Typical FIGAERO thermograms exhibit peaks ca. 40 °C  
225 wide, and thus a 35-point smoothing retains the main peak shape while reducing the influence  
226 of noise. In the constant temperature part of the thermogram (soaking period), signal levels  
227 change slowly with time, on average less than 5 % for a 35 points ( $\sim 3$  minutes) period, so a  
228 35-point smoothing is also appropriate. We note that the unsmoothed profiles are those that are  
229 normalized; smoothing relates only to determining the maximum signal values used for  
230 normalization.

231 The *ED* calculation from Eqn. 1 gives equal weight to all points in the thermogram. However,  
232 in a FIGAERO thermogram, equal weighting may not be appropriate. The desorption process has  
233 two stages, ramping and soaking, with the soaking period comprising approximately 70% of the  
234 time points in thermograms. However, most thermograms are featureless in the soaking period.  
235 In contrast, many thermograms exhibit a peak, or some otherwise characteristic behavior, in the  
236 ramping period. Since the behavior in the ramping period provides greater information as to the  
237 overall similarity between individual thermograms, we recommend down-weighting the soaking  
238 period such that the ramping and soaking periods ultimately carry approximately 4:1 weight in  
239 the calculation of the *ED*. We have tested weighting of 1:1, 2:1 and 10:1. Weighting of 4:1  
240 provides for the most robust clustering results for the example datasets. We do not recommend  
241 completely excluding the soaking period as this period still carries informational content  
242 (Schobesberger et al., 2018). Specifically, in calculating *ED* we use all data from the ramping  
243 period while down-weighting the data in the soaking period by calculating and using ten-point  
244 averages.

245 In summary, we calculate the *ED* based on the following steps: (i) smooth the original  
246 thermogram (with absolute signal) to find the maximum value; (ii) normalize the original  
247 thermogram to the smoothed maximum; (iii) average every 10 points in the soaking period; and  
248 (iv) calculate the *ED* between every two normalized, down-weighted thermograms.

### 249 **2.1.3. Dealing with noise**



250 Noise is an inherent property of any measurement. Noise in the FIGAERO thermograms  
251 results from various sources, including detector noise, background subtraction, and imperfect  
252 fitting of mass spectra. Noise influences the ED calculated between two thermograms, typically  
253 increasing the ED. Here, the level of noise,  $\xi$ , is characterized for each thermogram by calculating  
254 the average difference between the smoothed and unsmoothed normalized thermograms for  
255 the ramping period. The use of only the ramping period in assessing the noise level is consistent  
256 with the generally more characteristic behavior compared to the soaking period. The use of the  
257 normalized thermograms, rather than absolute, allows for comparison of noise between  
258 thermograms.

259 The noise level generally varies inversely with the fractional mass contribution of the ions,  
260 illustrated for a case study of the  $\alpha$ -pinene + OH SOA (Experiment 1 in **Table 1** and **Figure 1**). This  
261 indicates that ions contributing more to the total signal generally have a lower noise level.  
262 Detector noise is nominally independent of ion identity, and thus the low-signal ions have  
263 enhanced  $\xi$  after normalization.

264 Discussed further in section 2.3, clustering algorithms often perform poorly when overly  
265 noisy data are included in the clustering. This is especially the case for algorithms such as k-means  
266 and partitioning around medoids, which assign all the members to a cluster. Clustering methods  
267 that do not require assignment of all members, such as DBSCAN or our NSSC, are generally less  
268 sensitive to the influence of overly noisy members. However, we have found that the explicit  
269 exclusion of noisy thermograms up front serves to provide for more robust behavior and also  
270 removes the need to consider each noisy thermogram as a possible single-member cluster. The  
271 inclusion of overly noisy peaks might obscure the underlying structure of clustered thermograms.  
272 Noisy thermograms are identified as follows. First, the 5% of ions having the lowest noise are  
273 identified. The  $\xi$  value of the noisiest ion from this subset of low-noise ions is defined as the  
274 reference noise level,  $\xi_{ref}$ . Small differences in the choice of this threshold (e.g. using the lowest  
275 7% of ions) do not materially influence the results. Ions for which  $\xi_n > 3 \xi_{ref}$  are considered noisy  
276 and excluded from the initial clustering. For the experiments we examined, there are 88-120 out  
277 of ~300 ions left after noise screening, contributing 83.5% - 92.5% to the total particle mass.

278 **2.2. Noise-sorted Scanning Clustering (NSSC)**

279 **2.2.1. Algorithm description**

280 The noise-sorted scanning clustering (NSSC) algorithm developed here is a variant of the  
281 commonly used DBSCAN. In NSSC, identification and clustering of thermograms occurs based on  
282 their similarity to seed thermograms. When the  $ED$  between a given thermogram and the seed is  
283 less than a specified  $ED$  criterion ( $\epsilon$ ) the two members belong to the same cluster. Importantly,  
284 in NSSC the selection of the seed thermograms occurs based on their respective noise levels. The  
285 least noisy thermogram is selected as the initial seed, the next noisiest is selected as the second  
286 seed (assuming it is not already clustered), and so on. We have found that low-noise  
287 thermograms typically have more well-defined and characteristic shapes and comprise a  
288 substantial fraction of the total mass. The choice to select seeds based on the noise level leads  
289 to overall more robust and reproducible clustering compared to random selection of seeds.

290 The optimal value of the distance criterion,  $\epsilon$ , is not known *a priori*, but must be determined  
291 by the user, discussed in Section 2.2.3. A valid cluster must contain at least  $N_{min}$  members,  
292 inclusive of the seed. We use  $N_{min} = 2$ . Consideration and inspection of individual unclustered  
293 thermograms exhibiting unique behavior occurs as a post-clustering process (Section 2.2.2).

294 The flow of the noise-sorted scanning clustering algorithm is shown in **Figure 2** and  
295 summarized here. Clustering proceeds in two rounds. For the initial round, the thermograms are  
296 sorted by the noise ( $\xi$ ), and the  $ED$  values between all pairs of thermograms are calculated  
297 accordingly. All of the thermograms are identified according to whether they have been already  
298 used as seeds ( $SEED = 0$  or  $1$ , with  $1$  for thermograms used as seeds) and whether they have been  
299 already included in a cluster ( $CLUSTER = 0$  or  $1$ , with  $1$  for already clustered thermograms). At the  
300 start,  $SEED = 0$  and  $CLUSTER = 0$  for all thermograms. Clustering begins using the least noisy  
301 thermogram having  $SEED = 0$  and  $CLUSTER = 0$  as the initial seed. The state of that seed is then  
302 changed to  $SEED = 1$ . All thermograms having  $ED < \epsilon$  for that seed and with  $CLUSTER = 0$  are  
303 identified from the  $ED$  matrix; these thermograms are considered neighbors of the seed  
304 thermogram. The seed does not evolve as neighbors are added to the cluster during this step. If  
305 the number of neighbors plus the seed is greater than or equals  $N_{min}$ , the cluster is valid and

306 stored, with the states of all the thermograms in the cluster changed to CLUSTER = 1. Otherwise,  
307 the cluster is dismissed, and CLUSTER = 0 for all the members. In this case, the current seed (with  
308 SEED = 1 and CLUSTER = 0) will no longer be used as a seed in the future steps but can still end  
309 up clustered as a neighbor in the other clusters. The above steps are repeated until all the  
310 thermograms have either SEED = 1 or CLUSTER = 1.

311 Because a cluster must have at least  $N_{\min}$  elements, not all the thermograms may end up  
312 clustered. Some of these unclustered thermograms may nonetheless have very similar shapes to  
313 the clustered thermograms. Here, an iterative, second round of clustering potentially adds these  
314 initially unclustered thermograms to the initial clusters, using the signal-weighted average  
315 thermograms for the clusters from the first round as the initial seeds. A matrix of  $ED$  values is  
316 calculated between the individual unclustered thermograms and the new seeds. For each  
317 unclustered thermogram, the minimum  $ED$ , corresponding to only one of the seeds, is identified.  
318 When this minimum  $ED$  is less than  $\epsilon$ , the unclustered thermogram is added into that cluster. A  
319 new signal-weighted average thermogram for the cluster is calculated and this process repeats  
320 until no additional unclustered thermograms can be added to existing clusters. The mass  
321 contribution of the remaining unique unclustered thermograms after this second round can be  
322 substantial or negligible, ranging from <0.05% to 2.6% in the experiments presented here, and  
323 depends largely on the choice of  $\epsilon$ . Some of these unclustered thermograms are defined as  
324 additional one-member clusters, discussed in the following section.

### 325 **2.2.2. Post-clustering Processes**

326 After thermograms are clustered, we perform two post-clustering analyses to better  
327 understand the whole data set: 1) identifying additional one-member clusters and 2) sorting of  
328 the clusters.

329 Some of the remaining unclustered thermograms have significant individual mass  
330 contributions and should be considered as one-member clusters. The criterion of “significant”  
331 mass contribution is user-defined. We recommend determining the significance criterion as  
332 follows: (i) sorting all the ions (before the noise-filtering process) from largest to smallest  
333 individual mass concentration; (ii) calculating the cumulative mass fraction for this sorted list;

334 and (iii) defining as “significant” all those ions contributing to a cumulative mass contribution up  
335 to 80%.

336 The number of significant ions in a data set depends on the specific chemical system,  
337 varying from only a few to tens of ions. Significant unclustered ions are identified as additional  
338 one-member clusters. In some cases, the thermograms for these one-member clusters are  
339 unique compared to the previously identified clusters. In others, their shapes are visually similar  
340 to the previously identified clusters but where the one-member clusters are sufficiently distinct  
341 that they were not clustered. For the purpose of automation, these one-member clusters are all  
342 included in the final clustering results and the number of one-member clusters serves as one of  
343 the parameters to determine the optimal  $\epsilon$ . User can also choose to exclude them or some of  
344 them manually from the final clustering results based on their judgement. For the example  
345 systems considered in Section 4, there are only a few one-member clusters (ranging from 0 to 4),  
346 for the optimal  $\epsilon$  used.

347 Sorting of clustered thermograms facilitates visual presentation and identification of the  
348 similarities and dissimilarities among the clusters. The specific method of sorting can be varied  
349 depending on the application and system under consideration. Here, we use the temperature  
350 where 50% of the mass is desorbed ( $T_{m50}$ ) for the weighted-average cluster thermogram as a first  
351 criterion. The  $T_{m50}$  is typically similar to, but slightly larger than the temperature at which the  
352 signal reaches a maximum. As such, the  $T_{m50}$  is approximately related to the saturation vapor  
353 pressure of the desorbing compound, at least for compounds that desorb directly (e.g., Lopez-  
354 Hilfiker et al., 2014). When two or more clustered average thermograms have identical  $T_{m50}$ , a  
355 rare but occasional occurrence, they are further sorted by  $T_{m75}$ , the temperature where 75% of  
356 the mass is desorbed. The temperature difference between  $T_{m50}$  and  $T_{m75}$  indicates the slope of  
357 the thermogram between these two temperatures, with larger values indicating slower decay.  
358 Therefore, these two parameters generally illustrate the shape of a thermogram. The  $T_{m50}$  and  
359  $T_{m75}$  are determined by calculating the cumulative desorbed mass and finding the temperatures  
360 where 50% and 75% are reached.

361 The sorting process tends to organize the cluster-specific thermograms such that clusters  
362 having lower peak temperatures (lower  $T_{m50}$ ) and steeper downslopes after the peak (lower  $T_{m75}$ )

Deleted: , if any,

364 come first. Thermograms of this type are indicative of major contributions from higher-volatility  
365 monomers (Schobesberger et al., 2018). Thermograms having higher  $T_{m50}$  generally have broader  
366 peaks, and shallower downslopes, indicative of substantial contributions from low-volatility  
367 compounds or decomposition of oligomers. Further discussion of the interpretation of  
368 thermogram shapes is provided in Section 3.2.

### 369 2.2.3. Choosing the optimal $\epsilon$

370 NSSC is a distance-based clustering method, so the choice of the distance criterion,  $\epsilon$ , is a  
371 crucial step. For small  $\epsilon$ , members within a cluster have high similarity, but few thermograms end  
372 up clustered. In contrast, for large  $\epsilon$  the majority of the thermograms are clustered into only a  
373 few clusters having comparably low intra-cluster similarity. The choice of the optimal  $\epsilon$  value is  
374 guided here by consideration of several parameters that vary with  $\epsilon$ . The overall aim is to  
375 simultaneously (i) minimize the unclustered mass fraction ( $f_{m,unclustered}$ ) while (ii) maximizing the  
376 number of clusters ( $N_c$ ) having two or more members and (iii) minimizing the number of one-  
377 member clusters ( $N_{c,one}$ ) yet (iv) maintain inter-cluster separation ( $R_{interClst}$ ).

378 In general,  $N_c$  increases with  $\epsilon$  for small  $\epsilon$  because more thermograms of different shapes  
379 get clustered and fewer thermograms remain unclustered. As  $\epsilon$  further increases, some clusters  
380 are combined and a greater number of thermograms are assigned to a single cluster.  
381 Consequently, as  $\epsilon$  increases the  $N_c$  generally increases, reaches a maximum level, and then  
382 decreases. The maximum  $N_c$  and the  $\epsilon$  at which the maximum occurs depends on the exact size  
383 and the properties of dataset being examined. We have found that a typical SOA system usually  
384 has 9-13 distinct thermogram clusters. We recommend selecting an  $\epsilon$  that provides for  $N_c$  at or  
385 near the maximum as this captures the greatest number of thermogram types.

386 The mass fraction of unclustered thermograms,  $f_{m,unclustered}$ , includes only the unclustered  
387 thermograms that were not excluded based on the noise filtering. In general, a smaller  $f_{m,unclustered}$   
388 is preferable as this indicates a greater amount of the OA mass is included in a cluster (including  
389 one-member clusters). The  $f_{m,unclustered}$  generally decreases with  $\epsilon$ , then plateaus above a certain  
390 value of  $\epsilon$ ; ideally this plateau occurs at  $f_{m,unclustered} = 0$ . The  $\epsilon$  where the plateau starts is indicated  
391 as  $\epsilon_{MF}$ , where MF stands for mass fraction. Given that significant one-member clusters are

392 allowed, the unclustered thermograms that remain above  $\varepsilon_{MF}$  have individually small mass  
 393 contributions and are either truly unique in their shapes or have a sufficiently high noise level  
 394 that they cannot be clustered, even after the noise-screening process. We generally recommend  
 395 selecting  $\varepsilon \geq \varepsilon_{MF}$  to minimize the unclustered mass.

396 The number of one-member clusters,  $N_{c,one}$ , generally decreases with  $\varepsilon$ , as these ions are  
 397 incorporated into multi-member clusters. Ideally, these one-member clusters would exhibit clear,  
 398 visually distinct behavior compared to other one-member clusters and to multi-member clusters.  
 399 However, we find this is often not the case, especially at smaller  $\varepsilon$ . Thus, the number of one-  
 400 member clusters should generally be minimized; we suggest  $N_{c,one}$  be held to five or fewer in  
 401 general.

402 The inter-cluster separation parameter,  $R_{interClst}$ , characterizes the dissimilarity between  
 403 clusters, and is the ratio between the average inter-cluster distance ( $ED_{seed,avg}$ ) and  $\varepsilon$ , where:

$$404 \quad R_{interClst} = \frac{ED_{seed,avg}}{\varepsilon} = \frac{\sum_{i=1}^{N_{c,total}} \sum_{j=1}^{N_{c,total}} ED_{seed,i,j}}{N_{c,total}(N_{c,total}-1)\varepsilon} \quad (2)$$

406 and  $ED_{seed,i,j}$  is the distance between the seeds for the different clusters  $i$  and  $j$  and  $N_{c,total} = N_c +$   
 407  $N_{c,one}$ . For a 2D data set, the seed can be visualized as the center of a circle and  $\varepsilon$  the radius of  
 408 the circle. Thus, when  $ED_{seed,i,j}/\varepsilon < 2$ , the two circles defining the boundaries of these two clusters  
 409 have overlapping areas. Good separation (i.e. cluster dissimilarity) is indicated when  $ED_{seed,i,j}/\varepsilon >$   
 410  $2$ . Although our data set is more than two dimensions, this illustrates the idea of establishing the  
 411 level of similarity (or dissimilarity) between clusters, i.e., the extent to which they are unique. We  
 412 recommend selecting an  $\varepsilon$  that results in  $R_{interClst} \geq 2$ , when possible.

414 All four parameters should be considered when determining the optimal  $\varepsilon$ . Consideration  
 415 of the parameters individually may not result in the same optimal  $\varepsilon$ . Ultimately, the user must  
 416 consider each parameter and aim to select an optimal  $\varepsilon$  that balances the different information  
 417 provided in each parameter. This can be achieved by plotting the above parameters as a function  
 418 of  $\varepsilon$ , and then selecting as the optimal value the  $\varepsilon$  that results in (i) a small  $f_{m,unclustered}$  with (ii)  $N_c$   
 419 near the maximum and (iii) a small  $N_{c,one}$  and (iv)  $R_{interClst}$  near or above two. In addition, visual

420 comparison of the clustering results, illustrated as the average thermogram of each cluster, can  
421 be helpful. For the example data considered below, we find that the optimal  $\epsilon$  tends to fall within  
422 a relatively narrow range of values.

#### 423 2.2.4. Summary

424 The NSSC allows for clustering of ion peaks in temperature-dependent mass spectra  
425 measured by the FIGAERO-CIMS, from which mass thermograms of the different clusters are  
426 determined. The NSSC emphasizes contributions of ions having high signal-to-noise by selecting  
427 seeds for the mass spectral clusters according to decreasing signal-to-noise. The NSSC also  
428 accounts for the full temperature-dependent behavior of each ion, weighted towards the  
429 temperature ramping period during which the ions generally exhibit more characteristic  
430 desorption profiles. However, the NSSC requires as user input a distance criterion,  $\epsilon$ , which  
431 characterizes the minimum similarity required between a selected seed ion thermogram and all  
432 other (non-clustered) ion-specific thermograms for the non-seed ion to be considered part of the  
433 mass spectral cluster. The appropriate  $\epsilon$  value must be uniquely determined for a given  
434 experiment or set of experiments, but we recommend should be selected to provide both the  
435 greatest amount of clustered mass and number of mass spectral clusters having two or more  
436 members while also maintaining the greatest average separation between the mass spectral  
437 clusters. Altogether, these steps facilitate robust, reproducible determination of mass spectral  
438 clusters from a given data set.

Formatted: Font: Symbol

Formatted: Font: Symbol

#### 439 **2.3. Alternative Clustering Methods**

440 We have alternatively considered the performance of some of the most commonly used  
441 clustering algorithms (k-means, k-medoids, mean-shift, DBSCAN) and a less-commonly used one  
442 (FPClustering (Gonzalez, 1985)) for interpreting FIGAERO-CIMS observations. The clustering  
443 methods considered are summarized in **Table 2**, with some of their pros and cons listed, and  
444 described in further detail in Appendix A. We discuss them briefly here in the context of FIGAERO-  
445 CIMS data. All the methods considered require input of at least one key user-specified parameter.  
446 These parameters and the associated clustering algorithms can be generally classified into two  
447 categories: number-based and distance-based. Number-based clustering algorithms require

448 specifying the desired number of retrieved clusters; this includes k-means and k-medoids.  
449 Number-based algorithms usually assign all members to clusters. The extent of similarity among  
450 members of a cluster can vary greatly since there is no strict distance criterion for each cluster.  
451 When applied to FIGAERO-CIMS thermograms, we have found these number-based algorithms  
452 are particularly sensitive to the presence of noisy members and the initialization method. In  
453 contrast, some clustering algorithms require specification of distance (similarity) criterion. This  
454 includes the mean-shift, DBSCAN, and our NSSC algorithms. These distance-based algorithms  
455 need not cluster all members of the initial population and generally emphasize intra-cluster  
456 similarity or the density of the points. The methods differ in terms of the method used for  
457 selection of the initial seed or center and the extent to which they emphasize point density versus  
458 cluster similarity. Noisy members tend to naturally be excluded from any clusters. NSSC is a  
459 variant of DBSCAN. It does, however, differ from the standard DBSCAN algorithm because NSSC  
460 only searches for neighbors of the seed, while DBSCAN also searches for neighbors of the  
461 neighbors. In doing so, NSSC emphasizes cluster similarity rather than point density. This is  
462 particularly useful when clustering thermograms, as the behavior of the entire thermogram is  
463 considered; inclusion of neighbors of neighbors may cluster together thermograms that exhibit  
464 especially similar behavior in one region (e.g., the soaking period) but not another, an undesirable  
465 result. Accordingly, the sorting of seeds by noise levels is a key aspect of the NSSC algorithm,  
466 which we have found provides for more robust clustering results.

467 Most of these clustering algorithms, including k-means, k-medoids, and mean-shift, are  
468 initialized with a random choice of the initial cluster centers (or seeds). For large data sets, this  
469 randomness usually leads to different results of clustering with different runs. The extent to  
470 which this impacts analysis and clustering of FIGAERO-CIMS data is considered using SOA from  
471 the  $\alpha$ -pinene + OH SOA system as the case study (Section 4.1). For the FIGAERO-CIMS data we  
472 find that the various clustering results exhibit a moderate sensitivity to how the initial seeds are  
473 selected for all of these algorithms, although the final clusters are generally similar between  
474 different runs for the same input parameter. This may reflect either the relatively small size of  
475 the data set (~300 members originally and ~100 members after noise screening) or that there are  
476 generally characteristic peak shapes with overall good separation. However, some differences

Deleted: As such



478 between independent clustering runs result, which is undesirable. For FIGAERO-CIMS data we  
479 know that not all thermograms are of equal quality, i.e. they have different noise levels reflecting  
480 in part their different overall contributions to the total mass. The standard clustering methods  
481 do not account for this information. The NSSC algorithm developed here takes into account this  
482 measure of data quality and uses it to identify the seeds for clustering. This provides for an  
483 entirely reproducible clustering and generally emphasizes the behavior of the ions that  
484 contribute most to the FIGAERO-CIMS signal while still allowing for consideration of contributions  
485 of low-signal ions.

486 We find that different clustering algorithms can result in similar numbers of clusters with  
487 the cluster-averaged thermograms having visually similar shapes when each is run with  
488 appropriate user-selected parameters, although the details and robustness of each cluster vary  
489 method by method. The “appropriate” parameters however are different from the “optimal”  
490 parameters. There is usually different guidance for different algorithms on how to find the  
491 optimal parameters that result in the greatest similarity within clusters and dissimilarity among  
492 clusters. In the case of k-medoids, for example, the average silhouette indicates an optimal  
493 number of clusters of two for the case study system. Yet, this is certainly too few clusters based  
494 on the other methods.

495 In summary, we propose NSSC as the preferred algorithm in dealing with the FIGAERO data  
496 set based on: (i) the ability to generate similar results as the other commonly used clustering  
497 algorithms; (ii) good reproducibility and stability of results due to accounting for the noise of  
498 individual thermograms; (iii) good control over the similarity within the clusters by using a  
499 user-definable distance criterion; and (iv) a capability to identify unique thermograms as  
500 one-member clusters.

### 501 **3. FIGAERO Measurements and Experiments**

#### 502 **3.1. Instrument and experiment description**

503 The FIGAERO-CIMS instrument has been described previously in detail (Lee et al., 2014;  
504 Lopez-Hilfiker et al., 2014). A brief description is provided here, with some additional details in  
505 the Supplemental Material. The FIGAERO-CIMS measures the evolved gases from filter-collected

506 particles during temperature programmed thermal desorption. Thermal desorption of particles  
507 occurs in two-stages: a “ramping” and “soaking” period. During ramping, the temperature  
508 increases from room temperature to 200 °C, typically at 10 °C min<sup>-1</sup>. Most OA mass desorbs  
509 during the ramping stage. The temperature is held at 200 °C for ca. 30–40 mins during the soaking  
510 period to facilitate evaporation of the remaining, low-volatility organic mass from the filter. The  
511 evolved gas-phase compounds are measured using CIMS with the iodide (I<sup>-</sup>) reagent ion,  
512 appropriate for characterization of generally highly oxygenated components comprising most  
513 secondary organic aerosol (Lopez-Hilfiker et al., 2016; Isaacman-VanWertz et al., 2017; Lee et al.,  
514 2018). The resulting signal or mass concentration versus temperature (or equivalently time)  
515 curves for each ion constitute a thermogram. All individual thermograms are background  
516 corrected by subtracting the observed thermograms from appropriate blank experiments. The  
517 overall bulk thermogram is obtained by summing together the individual thermograms.

518 Several example applications of the clustering on FIGAERO-CIMS data are discussed in  
519 Section 4. These cover laboratory experiments on SOA derived from: (1) OH +  $\alpha$ -pinene and (2)  
520 OH +  $\Delta$ -3-carene, both at low-NO<sub>x</sub> conditions; (3) OH +  $\alpha$ -pinene as a function of [NO]; and (4)  
521 O<sub>3</sub> +  $\alpha$ -pinene, but where the SOA is allowed to isothermally evaporate at 80% RH for varying  
522 amounts of time prior to thermal desorption. These experiments are summarized in **Table 1**, with  
523 further details in the Supplemental Material and associated publications (D'Ambro et al., 2018;  
524 D'Ambro et al., 2019); all data are publicly available (Cappa et al., 2019). All the experiments were  
525 done in a 10.6 m<sup>3</sup> Teflon environmental chamber at Pacific Northwest National Laboratory (PNNL)  
526 (Liu et al., 2012; Liu et al., 2016).

### 527 **3.2. General interpretation of FIGAERO-CIMS thermograms**

528 This work focuses on development of the clustering method, rather than on interpretation  
529 of the FIGAERO-CIMS thermograms; an illustrative thermogram is shown in **Figure 3b**. However,  
530 discussion of the clustering results is aided by a general understanding of how FIGAERO-CIMS  
531 thermograms have been previously interpreted. Ions contributed by semi- and low-volatility  
532 compounds that desorb directly tend to exhibit strongly peaked, Gaussian-like thermograms with  
533 single-mode peaks between around 50 °C to 120 °C; the lower the peak desorption temperature  
534 ( $T_{\text{peak}}$ ) the higher the volatility of the desorbing compound (Lopez-Hilfiker et al., 2014; 2015). We

535 therefore refer to thermograms, or portions of thermograms, having this general shape as the  
536 “monomeric” content of the ion hereafter; direct evaporation of thermally stable dimers or other  
537 oligomers is possible, although will typically occur at higher temperatures due to the comparably  
538 lower volatility of these compounds. When multiple monomeric compounds having different  
539 vapor pressures contribute to the same ion, the resulting thermogram exhibits a broader peak  
540 and shallower slopes or, in particular cases, multiple, distinct peaks (Lopez-Hilfiker et al., 2015).  
541 However, very broad thermograms, especially those that peak at higher temperatures (> 120 °C  
542 or so), can also indicate contributions from thermal decomposition of very low-volatility  
543 monomers, dimers, and oligomers (Lopez-Hilfiker et al., 2015; Gaston et al., 2016; Schobesberger  
544 et al., 2018). Dimers and oligomers can evaporate directly, without thermal decomposition, as  
545 observed for isoprene-derived SOA (D’Ambro et al., 2017) and ambient monoterpene oxidation  
546 products (Mohr et al., 2017). However, fragments of dimers or oligomers are generally more  
547 abundant, indicating the importance of thermal decomposition for desorption of these low-  
548 volatility compounds. Both direct evaporation of extremely low-volatility compounds and  
549 decomposition of large molecules or oligomers can lead to high signal levels above ~120 °C. We  
550 refer to both peaks and the slowly varying signal above ~120 °C as the “oligomeric” content of  
551 the ion hereafter. We use the terms monomer and oligomer in a qualitative manner. A more  
552 quantitative analysis of the thermograms can help distinguish between direct evaporation,  
553 thermal decomposition, and the contributions of monomers versus oligomers (Schobesberger et  
554 al., 2018), yet is beyond the scope of the current work.

#### 555 **4. Example Applications**

556 To illustrate the broad utility of NSSC for interpretation and analysis of FIGAERO-CIMS data,  
557 we apply NSSC to the laboratory-generated SOA systems described above. The systems include:  
558 SOA formed from a single precursor under NO<sub>x</sub>-free conditions; SOA formed from a single  
559 precursor as a function of input [NO]; and, SOA formed from a single precursor with thermal  
560 desorption following isothermal evaporation.

561 **4.1.  $\alpha$ -pinene + OH SOA**

562 A total of 298 ions were characterized by FIGAERO-CIMS for SOA generated from the  
563  $\alpha$ -pinene + OH reaction (**Table 1**). Four ions were characterized as anomalous and excluded from  
564 further analysis (see Section 2.1.1). The mass concentration of each ion was calculated by  
565 integrating the signal across the entire desorption period and assuming an equal sensitivity of  
566 CIMS for all the compounds. The total mass concentration is the sum of all the non-anomalous  
567 ions. The mass spectrum and bulk thermogram of the remaining 294 ions are shown in **Figure 3**,  
568 with the bulk thermogram shown versus both temperature (**Figure 3b**) and time (**Figure 3c**) to  
569 illustrate the difference between the ramping and soaking periods. The individual thermograms  
570 exhibited a variety of shapes. The noise threshold for this data set was  $\zeta_{ref} = 0.020893$ . A total of  
571 188 ions were screened out via noise filtering. The remaining 106 ions contribute 92.5% to the  
572 total mass detected by FIGAERO-CIMS. The optimal  $\varepsilon$  was established through consideration of  
573 the co-dependencies of  $N_c$ ,  $N_{c,total}$ ,  $f_{m,unclustered}$  and  $R_{interClst}$  on  $\varepsilon$  (**Figure 4; Table 3**). For this data  
574 set, we determine the optimal  $\varepsilon = 2.6$ . Choice of a much smaller  $\varepsilon$ , around 1.5, gives a maximum  
575 in  $N_c$ , but leaves a large fraction of the mass unclustered. Choice of  $\varepsilon = 2.1$  or 2.2 yields larger  $N_c$   
576 and  $R_{interClst}$  than  $\varepsilon = 2.6$ , with a reasonably small  $f_{m,unclustered}$ . However, there is one type of  
577 thermogram (Clst#11 in **Figure 5**) that is only captured with  $\varepsilon \geq 2.6$  and this yields  $f_{m,unclustered} = 0$ .  
578 Using  $\varepsilon \geq 2.7$  also yields  $f_{m,unclustered} = 0$  and  $N_{c,one} = 0$ , but  $N_c$  and  $R_{interClst}$  decrease from  $\varepsilon = 2.6$ ,  
579 indicating increasing similarity between clusters with fewer types of shapes captured. The choice  
580 of  $\varepsilon = 2.6$  provides a compromise between maximizing  $N_c$ , minimizing  $f_{m,unclustered}$ , and keeping  
581  $R_{interClst}$  above two. The parameters and thresholds used for this data set are summarized in **Table**  
582 **3**.

583 A total of 11 clusters are identified with no one-member clusters. The unweighted and  
584 mass-weighted average thermograms for each cluster are shown along with the thermograms of  
585 individual members in **Figure 5a**. The differences between weighted and unweighted average  
586 clusters are negligible, in general. Clusters are organized and numbered (as Clst#*N*) from low to  
587 high  $T_{m50}$ , with deeper to shallower downslope. Clst#1 through Clst#6 all have a clear peak below  
588 120 °C, but with different peak widths and downslopes. Clst#7 and Clst#8 are a bit noisier with

589 only a few members each, exhibiting a sharp upslope and shallow downslope. Clst#9 has a very  
590 broad peak. Clst#10 peaks at around 150 °C after an initial rise and temporary plateau. Clst#11  
591 exhibits behavior somewhat like Clst#10, but with a peak that occurs just into the soaking period,  
592 evident if viewed in time space, at 200 °C with a rapid drop afterwards.

593 The total mass concentration of a given cluster ( $M_{C,N}$ ) is the sum across all cluster members,  
594 calculated by integrating the summed mass concentration across the entire desorption period.  
595 The percentage mass contribution of each cluster, and of the unclustered and the noise-filtered  
596 ions, as well as the number of members for each cluster are shown in **Figure 5b** and **Table S1**.  
597 Clst#2 and Clst#3 contain the majority of the mass (20.1% and 44.3%, respectively) and consist  
598 of nearly half of the clustered ions (11 and 42, respectively). Clst#4 and Clst#9 also contain a  
599 notable percentage of the total mass (8.2% and 9.8%, respectively) and include a notable number  
600 of ions (13 and 17, respectively). Other clusters contribute relatively little to the total mass and  
601 contain a small fraction of ions.

602 The mass-weighted average molecular formulas ( $C_xH_yO_zN_m$ ) differ between clusters, as do  
603 the O:C and H:C atomic ratios (**Table S1**). There is no clear relationship between  $T_{m50}$  (or cluster  
604 number) and the number of carbon atoms, MW, or O:C. There is, however, a reasonable, inverse  
605 correlation between  $T_{m50}$  and H:C ( $r^2 = 0.78$ ). The number of carbon atoms is notably larger for  
606 Cluster 6 ( $x = 11.1$ ) and Cluster 7 ( $x = 15.3$ ); if those two clusters are excluded there is an inverse  
607 relationship between  $T_{m50}$  and the number of carbon atoms ( $r^2 = 0.79$ ) and with MW ( $r^2 = 0.59$ ).  
608 While the reason for these two clusters having comparably large numbers of carbon atoms is  
609 unknown, this nonetheless suggests that the contribution of oligomer decomposition might  
610 increase for clusters having higher  $T_{m50}$  values.

611 Interpretation of previous FIGAERO-CIMS studies have largely focused on the behavior of  
612 the bulk thermogram or of several major ions or sums of ions based on common factors such as  
613 the number of carbon atoms (Lopez-Hilfiker et al., 2016; D'Ambro et al., 2017; D'Ambro et al.,  
614 2018; Stolzenburg et al., 2018; Wang and Ruiz, 2018; Joo et al., 2019). The normalized  
615 thermograms of the top five ions contributing most to the total mass for the experiments here  
616 are shown in **Figure 5c**, along with the bulk thermogram. Together these five ions make up nearly  
617 30% of the total mass, and exhibit very similar thermogram shapes to each other and to the bulk

618 thermogram and belong solely to either Clst#2 or Clst#3. Thus, examining these ions only would  
619 capture only a fraction of the overall diversity in thermal behaviors. The clustering method  
620 developed here provides a means to investigate more comprehensively the variability in volatility  
621 between aerosol components.

#### 622 **4.2. $\Delta$ -3-carene + OH SOA**

623 A total of 298 ions were characterized by FIGAERO-CIMS for SOA generated from the  
624 reaction of  $\Delta$ -3-carene + OH (Table 1). Five were identified as having anomalous thermograms  
625 and excluded from further analysis. The mass spectrum and bulk thermograms of  $\Delta$ -3-carene +  
626 OH SOA are shown in Figure 6. Compared to the  $\alpha$ -pinene +OH SOA described above, the mass  
627 spectrum of  $\Delta$ -3-carene SOA is quite different, with one ion ( $C_8H_{12}O_5$ ) dominant. The bulk  
628 thermograms of the two SOA systems both look bell-like, but with the  $\Delta$ -3-carene SOA  
629 thermogram having a peak temperature ca. 9 °C higher. After noise-filtering, 110 ions remained  
630 for clustering, contributing 90.7% to the total mass. The optimal  $\varepsilon = 2.1$ , established again by  
631 considering the system-specific dependence of  $N_c$ ,  $N_{c,one}$ ,  $f_{m,unclustered}$  and  $R_{interClst}$  on  $\varepsilon$  (Figure S1),  
632 with the parameters and thresholds summarized in Table 3.

633 Ten clusters are identified, including one one-member cluster, with thermograms shown in  
634 Figure 7a and the mass contribution and number of ions in a cluster in Figure 7b. Chemical  
635 properties of each cluster are summarized in Table S2. The general characteristics of  
636 thermograms identified in the  $\Delta$ -3-carene + OH SOA are similar to those of low- $NO_x$   $\alpha$ -pinene +  
637 OH SOA described above, but with different mass contributions. For example, Clst#4 has nearly  
638 identical shape of the thermogram as Clst#3 in the  $\alpha$ -pinene SOA but contributes less to the total  
639 mass, 28.0% compared to 44.3%. Clst#6 in the  $\Delta$ -3-carene SOA contributes 14.8% to the total  
640 mass and resembles Clst#5 in the  $\alpha$ -pinene SOA, which contributes only 4.0% to the total mass.

641 In general, Clst#1 – 6 in the  $\Delta$ -3-carene SOA all exhibit a peak below 120 °C, with clear peaks  
642 of varying width and downslopes of varying steepness, but nominally in order of narrow to wide  
643 and steep to shallow, respectively. These clusters carry the majority of the desorbed mass. Clst#7  
644 and Clst#8 both exhibit relatively flat thermograms in the ramping period after their initial rise,  
645 and contribute 9% to the total mass. Clst#9 has a peak temperature above 150 °C and Clst#10

646 reaches a maximum during the soaking period. These last two clusters contribute little to the  
647 total mass (0.6% and 0.3%, respectively).

648 The thermograms of the five largest ions are shown in **Figure 7c**. These five ions together  
649 carry ~35% of the SOA mass. A wider variety of thermogram shapes are captured by the top five  
650 ions compared to the  $\alpha$ -pinene SOA system. However, thermograms characteristic of Clst#7–10  
651 are not represented by these top five ions; this remains true even if the top 10 ions are  
652 considered (not shown).

653 There are ultimately three major differences between the two SOA systems. For one, there  
654 is a different relationship between fractional contribution and cluster number (and thus  $T_{m,50}$ )  
655 between the two. Secondly, the  $\alpha$ -pinene SOA contains ions with especially narrow peaks at ca.  
656 100 °C (i.e., Clst#7 & 8), that are not observed with  $\Delta$ -3-carene SOA (compare **Figure 5** with **Figure**  
657 **7**). Lastly, the thermograms of the top five ions for  $\Delta$ -3-carene SOA differ to a greater extent than  
658 for  $\alpha$ -pinene SOA. Although we are unable to determine the reasons for these differences here,  
659 this illustrates the potential for clustering to help identify and understand differences between  
660 different SOA systems.

#### 661 **4.3. $\alpha$ -pinene + OH + NO SOA**

662 Thermograms from SOA generated from the reaction of  $\alpha$ -pinene + OH at varying NO  
663 concentrations (5 ppb, 10 ppb and 25 ppb; **Table 1**) are considered as a set of experiments.  
664 Together, differences between them illustrate the impact of changes to the fate of RO<sub>2</sub> peroxy  
665 radical intermediates on the SOA composition and thermal properties (Praske et al., 2018; Zhao  
666 et al., 2018). Clustering proceeds here using two complementary approaches. In the single  
667 clustering method, clustering is performed for one reference experiment (i.e., at one NO  
668 concentration, 5 ppb, Expt#3a). Then, average thermograms are calculated for the other  
669 experiments in the set using the same cluster members as identified in the reference experiment.  
670 In the multiple clustering method, clusters are independently determined for each experiment in  
671 the set, and the shapes, relative abundances, and contributing ions are compared between  
672 experiments. For all three experiments, the same initial set of 298 ions were characterized by  
673 FIGAERO-CIMS.

#### 674 4.3.1. Single Clustering

675 The ions identified as anomalous in each experiment differed. This most likely results from  
676 shifts in the background signal levels between experiments. To maintain consistency between  
677 the three experiments, ions identified as anomalous in any of the experiments were excluded  
678 from all the experiments, with four ions excluded in total. A total of 88 ions were kept for  
679 clustering after noise-filtering using the 5 ppb NO reference experiment, contributing 84.5% to  
680 the total mass. The optimal  $\epsilon = 2.2$  (**Figure S2** and **Table 3**), resulting in ten clusters with one  
681 one-member cluster. The same sets of ions were then used to calculate the cluster-average  
682 thermograms for the 10 ppb and 25 ppb NO experiments. Chemical characteristics of the clusters  
683 are summarized in **Table S3**.

684 Mass spectra for the three experiments are compared in **Figure 8a** and the bulk  
685 thermograms shown in **Figure 8b** and **c**. The 5 ppb NO and 10 ppb NO SOA mass spectra are  
686 nearly identical. The mass spectrum for the 25 ppb NO experiment, however, exhibits a notable  
687 shift of the most abundant ions towards lower  $m/z$ . The bulk thermograms for the 5 ppb and 10  
688 ppb NO experiments are nearly identical, peaking near 80 °C. The 25 ppb NO bulk thermogram  
689 similarly peaks near 80 °C, but exhibits a much slower decay as temperature increases further.  
690 Additionally, the change in slope at the transition from the ramping to soaking period is more  
691 pronounced in the 25 ppb NO experiment. Overall, a greater fraction of the mass desorbs above  
692 100 °C and during the soaking period for the 25 ppb NO experiment compared to lower-NO  
693 experiments.

694 Despite the differences in the bulk thermograms, the shapes of the weighted-average  
695 thermograms of clusters for all the NO experiments are generally similar, with the exception of  
696 Clst#6 (**Figure 9a**). In particular, the 25 ppb thermogram shape of Clst#6 differs substantially from  
697 those of low-NO conditions, with a much reduced initial peak (around 80 °C) and an more  
698 pronounced second peak at high temperature (around 200 °C). However, this cluster contributes  
699 negligibly to the overall mass. There is some suggestion of similar behavior for Clst#10, although  
700 to a lesser extent. For the three most abundant clusters, Clst#1, 2 and 4, there is a slightly  
701 increased relative contribution of the 100-200 °C tail for 25 ppb NO, consistent with differences  
702 in the bulk thermograms.



703 The most notable NO-dependent change is in the relative abundances of the clusters  
704 between the 5 and 10 ppb NO experiments and the 25 ppb NO experiment (**Figure 9b**). The  
705 cluster mass fractions are nearly identical between the 5 and 10 ppb NO experiments. The  
706 relative contributions of higher-number clusters (which have been ordered according to  
707 increasing  $T_{m,50}$ ) increase for the 25 ppb NO experiment. This is consistent with the increased  
708 persistence of the 25 ppb NO bulk thermogram to higher temperatures and the nearly identical  
709 nature of the 5 ppb and 10 ppb NO bulk thermograms (**Figure 8b**). The clustering analysis suggests  
710 that differences in the bulk thermogram arise from shifts in the relative contributions of the  
711 various SOA components that result from the altered photochemical environment. These  
712 observations generally suggest an increasing fraction of oligomeric content, or less-volatile  
713 compounds, formed in the particle phase—or potentially the gas phase—when the SOA was  
714 generated under higher chamber NO conditions (Schobesberger et al., 2018).

#### 715 **4.3.2. Multiple Clustering**

716 With multiple clustering, each experiment was processed and clustered independently,  
717 with experiment-specific  $\zeta_{ref}$ ,  $N_c$ , and  $\varepsilon$ , among other parameters (**Figure S4** and **Table 3**). The  
718 clustered thermograms from the three experiments are compared in **Figure 10a-c**. The number  
719 of clusters identified increases with NO concentration. Comparison between the shapes of the  
720 clusters from the 5 ppb NO (**Figure 10a**) and 10 ppb NO (**Figure 10b**) experiments indicates  
721 generally similar types of thermograms, consistent with the single clustering method. Ten of the  
722 11 total 10 ppb clusters match with a 5 ppb cluster. The one additional, unique cluster at 10 ppb  
723 NO (Clst#9), is a one-member cluster with a sharp, narrow peak at low temperatures and a  
724 broader, shallow second peak at high temperatures. This ion was filtered out due to high noise  
725 level in the 5 ppb NO experiment.

726 The 25 ppb NO experiment (**Figure 10c**) results in more clusters compared to the lower NO  
727 experiments; 13 for the 25 ppb NO experiment versus 10 and 11 for the 5 and 10 ppb experiments,  
728 respectively. Some of the 25 ppb NO clusters have shapes similar to the lower NO experiments,  
729 but many differ substantially. For example, two of the unique 25 ppb NO clusters (Clst#12 and  
730 #13) have thermograms for which the signal increases continuously through the ramping period

731 and even into the soaking period. These clusters were not found in the single clustering analysis  
732 because the 5 ppb NO experiment was used as the reference.

733 The new types of thermograms observed in the 25 ppb NO experiment indicates either  
734 formation of new compounds or a change in the relative contributions of different components  
735 to the same ions. Either could result from a change in the fate of the peroxy radical intermediates  
736 as the NO concentration increases, leading to notably different products. There were numerous  
737 nitrogen-containing ions observed for the three experiments. These N-containing ions belong to  
738 Clst#1 – 7 for all the three [NO] conditions (**Table S4**). The higher-number clusters did not include  
739 N-containing ions, also indicating a limited influence of the N-containing products on these lower-  
740 volatility thermograms, although fragmentation complicates the interpretation. Overall, the  
741 formation of new N-containing compounds at the high NO condition does not seem to explain  
742 the unique thermograms in the 25 ppb NO experiments.

743 The percent contribution of different clusters to total mass, along with the noise-filtered  
744 and unclustered ions, differ between experiments (**Figure 10d**). Note that for the multiple  
745 clustering method, clusters having the same index number are not necessarily directly  
746 comparable between experiments because different sets of ions are included. For example, while  
747 Clst#1 in the 5 ppb and 10 ppb NO experiments are comparable, the most similar cluster in the  
748 25 ppb experiment is Clst#2. Nonetheless, there are some common features shared by the same,  
749 or closely indexed, clusters. For example, Clst#1 – 4 in all three experiments exhibit a narrow,  
750 single peak with the peak temperature below 120 °C. The mass contribution of Clst#1 – 4 is similar  
751 between the 5 and 10 ppb NO experiment, but ~15% lower in the 25 ppb NO experiment. Clusters  
752 that reach their maximum signal at or above 150 °C (Clst#9, 10 for 5 ppb, Clst#10, 11 for 10 ppb  
753 and Clst#10 – 13 for 25 ppb) together contribute ~6% in the low NO experiments and ~13% in  
754 the high NO experiments. Thus, there is some evidence that at higher NO there is an increased  
755 contribution of oligomeric compounds, indicated by the increased contribution of clusters that  
756 peak at higher temperatures and exhibit broader overall thermograms. However, overall these  
757 observations suggest complex shifts in the distribution of products, both monomeric and  
758 oligomeric, with sufficient increases in NO to change the fate of the peroxy radical intermediates.

759 **4.4.  $\alpha$ -pinene + O<sub>3</sub> SOA**

760 SOA formed from dark ozonolysis of  $\alpha$ -pinene was collected and then allowed to  
761 isothermally evaporate for varying amounts of time (0 h, 1 h, 3 h, 6 h and 24 h) before thermal  
762 desorption (**Table 1**, Expt#4). As above for the SOA formed at varying NO concentrations, these  
763 experiments are considered as a set and interpreted using both the single-clustering and  
764 multiple-clustering approaches. The single-clustering approach uses the 0 h (no-wait) experiment  
765 as the reference for initial clustering. In this set of experiments, 312 ions were characterized by  
766 FIGAERO-CIMS for each experiment.

767 **4.4.1. Single Clustering**

768 Only a few ions, if any, were identified as anomalous in each experiment; a total of ten ions  
769 were removed from all the experiments to maintain consistency between experiments. The mass  
770 spectra and bulk thermograms of the remaining 302 ions for the five experiments are shown in  
771 **Figure 11**. As the isothermal evaporation time increases, the mass spectrum changes significantly,  
772 as previously reported by D'Ambro et al. (2018). In the no-wait experiment, the mass spectrum  
773 is dominated by one ion, C<sub>10</sub>H<sub>14</sub>O<sub>6</sub>. Upon isothermal evaporation, the relative abundance of this  
774 ion notably decreases, with the extent of decrease increasing with wait time; over time, a greater  
775 number of ions contribute to the total mass, both at lower and higher  $m/z$ . With isothermal  
776 evaporation, the bulk thermograms also exhibit a shift from a more peaked shape, reminiscent  
777 of that from a single compound (Lopez-Hilfiker et al., 2014), to a more flattened peak with a  
778 shallower rise (**Figure 11**). In other words, with increasing isothermal evaporation the majority  
779 of the mass desorbed during thermal desorption shifts from a lower to higher temperature region.  
780 This behavior largely reflects the loss of comparably more volatile compounds during isothermal  
781 evaporation, leaving behind SOA that is overall less volatile (**Figure S6a**). It can also in part be due  
782 to higher molecular weight, lower volatility compounds being produced with time via accretion  
783 reactions in the condensed phase.

784 There are 12 clusters determined from the no-wait experiment, exhibiting a wide variety of  
785 the shapes (**Figure 12a**), with the parameters used for data pre-processing and clustering  
786 reported in **Table 3** and shown in **Figure S5**. Focusing first on the no-wait experiment, the cluster

787 thermogram shapes include those having clear peaks at relatively low temperatures (~60 °C) and  
788 with a sharp rise and fall (e.g., Clst#1-3), those having sharp peaks at relatively low temperatures  
789 but with a shallow downward slope (e.g., Clst#6), those with a broad peak at somewhat higher  
790 temperatures (~100 °C) and long tails (e.g., Clst#7), and those having a wide peak at even higher  
791 temperatures ~120 °C with a very broad rise and fall (e.g., Clst#10).

792 Changes to the shapes of the thermograms that occur upon isothermal evaporation differ  
793 between the clusters. Some of the clusters exhibit almost step changes from the no-wait to the  
794 longer time experiments (e.g., Clst#2 and 6), while others exhibit more continuous changes (e.g.,  
795 Clst#3 and 5). However, in all cases the clusters shift to have peaks that occur at higher  
796 temperatures with generally broader thermograms. In other words, the  $T_{m50}$  of all the clusters  
797 increase as a function of evaporation time, but with larger increases observed for the clusters  
798 having initially lower  $T_{m50}$  (**Figure 12b**). For some of the clusters with a clear peak below 100 °C,  
799 such as Clst#1–6, the peaks broaden to become less obvious and shift to higher temperatures  
800 with longer isothermal evaporation. For clusters that originally have very wide peaks, such as  
801 Clst#8–10 and 12, isothermal evaporation engenders a general shift in the thermograms towards  
802 higher temperatures. Different from the clusters described above, thermograms for two clusters,  
803 Clst#7 and Clst#11, exhibit only minor shift of peak temperature and shapes. Thermograms of  
804 these two clusters share the common features of a moderate-width peak that reaches a  
805 maximum between 100 – 120 °C. The  $T_{m50}$  of these two clusters correspondingly exhibit small  
806 changes compared to other clusters.

807 Isothermal evaporation generally leads to a reduction of the monomeric character of  
808 clusters, leaving behind components that exhibit increased oligomeric content. Differences in  
809 how the individual cluster thermograms evolve with isothermal evaporation are therefore likely  
810 indicative of differing relative contributions of monomeric versus oligomeric components. For  
811 example, Clst#1 and Clst#10 have distinctly different shapes in the 0-h wait experiment, but very  
812 similar shapes in the 24-h wait experiment. This indicates that ions in Clst#1 are not contributed  
813 from a single component, as might be inferred from the single-mode peak in the 0-h wait  
814 experiment. Instead, they are contributed by multiple components, though initially dominated  
815 by monomeric compounds, so the shift in peak temperature and broadness is substantial. On the

816 other hand, ions in Clst#10 must also derive from multiple components, but with only a small  
817 fraction of monomeric compounds that evaporate in the 24 hours. Consequently, the loss of  
818 low-temperature mass is apparent yet small. In contrast, ions in clusters such as Clst#7 and 11  
819 must be composed of only low-volatility components because they exhibit minimal changes in  
820 the thermograms shapes.

821 The extent of mass loss with isothermal evaporation differs between clusters. In general,  
822 clusters that exhibit larger changes in shape have greater total mass loss, although with variability  
823 (Figure S6c). Consequently, the mass contributions of the clusters evolve with isothermal  
824 evaporation (Figure 12b). The contribution of Clst#1 decreases significantly and most notably as  
825 wait time increases. The most prominent ion in the no-wait experiment,  $C_{10}H_{14}O_6$ , is grouped in  
826 Clst#1. The continuous mass loss of Clst#1 indicates the rapid evaporation of its members. The  
827 mass contributions of the other clusters that exhibited similar changes in shape as Clst#1 (Clst#3,  
828 5, and 6) remain comparably constant, although with Clst#3 decreasing slightly. The relative  
829 abundances of the clusters for which the thermograms shapes changed negligibly (Clst#7 and 11)  
830 increase continually, implying of the slowest evaporation of the ions in these two clusters in the  
831 24-hr evaporation period.

832 For comparison, D'Ambro et al. (2018) reported changes in the shapes of the thermograms  
833 for the five most abundant individual ions from the no-wait to 24-hr experiment, together  
834 carrying ~15% of the particle mass. They observed the individual ion thermograms generally all  
835 evolved in a manner similar to our Clst#1, 3 and 5, shifting from narrower, more peaked profiles  
836 towards broader profiles with a shallower rise, less evident peak, and increased evaporation at  
837 higher temperatures. Here, with the clustering of data, we are able to track the change of thermal  
838 behaviors of ions carrying ~87% of the initial mass. We are able to confirm that ~70 % of the mass  
839 exhibit similar thermal behaviors and responses to isothermal evaporation as the top five ions.  
840 However, we are also able to identify another ~17% of the mass having initial thermograms not  
841 characterized by the top five ions, including 12% of the mass (Clst#7 and 11) that behaves  
842 distinctly different upon evaporation at room temperature.

#### 843 4.4.2. Multiple Clustering

844 The number of clusters identified with the multiple-clustering method, using experiment-  
845 specific optimal  $\varepsilon$  values (**Table 3** and **Figure S7**), decreases with isothermal evaporation time,  
846 from 13 (no-wait) to 12 (1 h) to 11 (3 h) and then to 9 (6 h and 24 h) (**Figure 13b-f**). The noise  
847 levels of the thermograms increase with evaporation time due to decreasing absolute particle  
848 mass. Nonetheless, the typical shapes of the cluster-specific thermograms clearly evolve with  
849 increasing isothermal evaporation. For short isothermal evaporation times, many cluster-specific  
850 thermogram profiles are relatively narrow, peaking at lower temperatures (70-120 °C) and with  
851 rapid rises and evident downslopes. For longer isothermal evaporation times, the cluster-specific  
852 profiles instead have broad peaks with slow rises and most of the mass desorbing at higher  
853 temperatures.

854 To aid further general interpretation, the cluster-specific thermograms with  $T_{m50} < 120$  °C  
855 are grouped together as higher-volatility clusters. The number of higher-volatility clusters  
856 decreases with isothermal evaporation, from ten for the no-wait experiment, to five in the 1-h  
857 experiment, two in the 3-h and 6-h experiment, to none in the 24-h experiment (**Figure 14**). The  
858 mass contributions of the higher-volatility clusters decrease from 81.9% to 60.4%, 17.2%, 9.4%  
859 and to 0.0%, with increasing isothermal evaporation time. This overall behavior is consistent with  
860 results from the single-clustering method and indicates the compounds with a wide range of  
861 volatilities make up much of the mass in the initial particles, while the SOA after isothermal  
862 evaporation is composed of compounds having lower volatilities.

863 After isothermal evaporation, some cluster-specific thermograms have signals that increase  
864 continuously during the ramping period, for example Clst#11 and 12 in the 1-h experiment; such  
865 clusters were not observed in the no-wait experiment. The relative abundance of these very low-  
866 volatility clusters increases with isothermal evaporation, from 1.7% in the 1-h experiment  
867 (Clst#11 and 12) to 13.4% in the 24-hr experiment (Clst#7 and 9). The absence of these clusters  
868 for the no-wait experiment suggests that they are formed over time through condensed-phase  
869 reactions. Their increasing contribution over time may reflect both evaporation of higher  
870 volatility components and continued formation. Clusters having thermograms with very broad  
871 peaks, such as Clst#11 and 13 in the 0-h experiment are also observed in all the other experiments,  
872 with increasing contribution to the total mass.

873 The multiple-clustering method reveals the disappearance of certain types of thermograms,  
874 (e.g., the no-wait Clst#3) and the emergence of other types of thermograms (e.g., the 1-h Clst#11)  
875 as evaporation time increases. This complements the single-clustering method, which illustrates  
876 gradual changes in the shapes of cluster-specific thermograms, by allowing for identification of  
877 completely new thermogram shapes and divergent behavior between ions within initial clusters.  
878 The multiple-clustering method also confirms the decrease of the diversity of the desorption  
879 profiles, as suggested by the single-clustering method. The two methods complement each other  
880 and together provide a detailed look into (i) how the desorption profiles of sets of ions evolve  
881 with isothermal evaporation and (ii) how the fraction of different types of thermograms change  
882 with evaporation time.

## 883 **5. Conclusions**

884 We developed a new clustering algorithm, the noise-sorted scanning clustering (NSSC)  
885 algorithm, for application to FIGAERO-CIMS data sets. The NSSC algorithm provides a robust  
886 method for clustering of FIGAERO-CIMS thermograms having distinct thermal desorption profiles  
887 and of determining the mass contribution of each cluster. Each of the ions contributing to a  
888 cluster results from one or more molecules sharing similar thermochemical properties. These  
889 molecules either evaporate directly or decompose and then evaporate. Compared to other  
890 existing clustering algorithms, NSSC is strictly similarity-based, reproducible, and takes into  
891 consideration differences in noise levels between individual ions. The application of NSSC has the  
892 potential to make FIGAERO data more accessible to the atmospheric chemistry community.

893 For the four different SOA systems we examined, more than 80% of the total mass is  
894 clustered, with the number of clusters ranging from 9 to 13. The shapes of the cluster-specific  
895 average thermograms exhibit substantial variation for a given system. Some have relatively sharp  
896 peaks, others broad peaks with slowly decreasing signal as heating continues, and others still  
897 having signals that continually increase up to very high temperatures or long desorption times.  
898 The mass contribution of a cluster varies from 0.2% to 44.3%. A few (2-3) clusters usually contain  
899 more than 50% of the total mass in all the chemical systems examined. Comparison of the cluster-

900 specific thermogram shapes between different SOA systems allows for qualitative assessment of  
901 the similarity or uniqueness.

902 We also demonstrated the potential of the NSSC for guiding interpretation of sets of  
903 experiments where one experimental condition varies (e.g., NO concentration and evaporation  
904 time). For such experiments, two complementary methods are suggested: (i) the single clustering  
905 method, where one experiment is used to determine the ions belonging to individual clusters  
906 and then clusters comprising the same ions are calculated for the other experiments, and (ii) the  
907 multiple clustering method, where each experiment is clustered independently and then  
908 compared. The first approach helps establish how the properties of individual clusters evolve as  
909 a set, while the second approach helps identify changes in the diversity of cluster-specific  
910 thermogram shapes, properties, and mass contributions. The two approaches complement each  
911 other and provide guidance for future efforts to cluster ambient observations having long time-  
912 series.

913 This paper focuses only on the description of the clustering algorithm and its potential as a  
914 tool to characterize the thermal properties of organic aerosol in further detail. [The application of  
915 NSSC can be potentially expanded to any other composition-resolved data sets, such as diurnal  
916 changes of different compounds measured in ambient air, temporal changes of different  
917 generations of species in a smog chamber, and composition-dependent size distributions. All of  
918 the above data sets share a common property that the noise of the curve/spectrum is related to  
919 the composition. Therefore, NSSC would facilitate the analysis by taking noise into consideration.](#)  
920 Interpretation of the cluster-specific thermograms using frameworks such as that of  
921 Schobesberger et al. (2018) will allow for more comprehensive understanding of the  
922 thermochemical properties of the organic aerosol, the subject of future work. This will provide  
923 insights into the thermal behavior of organic aerosol and the relative contributions of thermally  
924 stable (e.g., monomer) versus thermally unstable (e.g., dimers or oligomers) compounds, the  
925 volatility distribution of the thermally stable compounds, and the T-dependent rate coefficients  
926 for oligomer dissociation and formation.



## 927 **6. Data Availability**

928 All data and the NSSC algorithm used in this publication are archived in the UC DASH data  
929 repository (Cappa et al., 2019). The NSSC algorithm is also available at GitHub  
930 (<https://github.com/chriscappa/NSSC>), with the version used for this publication available as Li  
931 and Cappa (2019).

## 932 **7. Author Contributions**

933 ZL developed the NSSC algorithm. ELD, SS, CJG, FDL-H, JL, JES, and ZL performed  
934 measurements. ELD and SS performed detailed data processing. ZL and CDC analyzed data and  
935 wrote the manuscript, with contributions from all co-authors.

## 936 **8. Acknowledgements**

937 This work was supported by the National Science Foundation under Grant No. ATM-  
938 1151062. The experimental work described here was supported by the U.S. Department of  
939 Energy ASR grants DE-SC0011791 and DE-SC0018221. E.L.D. was supported by the National  
940 Science Foundation Graduate Research Fellowship (grant no. DGE-1256082) and S.S. was  
941 supported by the Academy of Finland (grant nos. 272041 and 310682). The SOAFFEE campaign  
942 was done at Pacific Northwest National Laboratory, supported by the U.S. Department of Energy  
943 (DOE) Office of Science, Office of Biological and Environmental Research, as part of the  
944 Atmospheric Systems Research (ASR) program. PNNL is operated for DOE by Battelle Memorial  
945 Institute under contract DE-AC05-76RL01830.

## 946 **9. References**

947 Abdalmogith, S. S., and Harrison, R. M.: The use of trajectory cluster analysis to examine the long-  
948 range transport of secondary inorganic aerosol in the UK, *Atmos Environ*, 39, 6686-6695,  
949 <https://doi.org/10.1016/j.atmosenv.2005.07.059>, 2005.  
950 Beddows, D. C. S., Dall'Osto, M., and Harrison, R. M.: Cluster Analysis of Rural, Urban, and  
951 Curbside Atmospheric Particle Size Data, *Environ Sci Technol*, 43, 4694-4700,  
952 <https://doi.org/10.1021/es803121t>, 2009.  
953 Cape, J. N., Methven, J., and Hudson, L. E.: The use of trajectory cluster analysis to interpret trace  
954 gas measurements at Mace Head, Ireland, *Atmos Environ*, 34, 3651-3663,  
955 [https://doi.org/10.1016/S1352-2310\(00\)00098-4](https://doi.org/10.1016/S1352-2310(00)00098-4), 2000.

956 Cappa, C. D., Li, Z., D'Ambro, E. L., Schobesberger, S., Shilling, J. E., Lopez-Hilfiker, F., Liu, J., Gaston,  
957 C. J., and Thornton, J. A.: Initial application of the noise-sorted scanning clustering algorithm to  
958 the analysis of composition-dependent organic aerosol thermal desorption measurements, UC  
959 Davis Dash, Dataset, <https://doi.org/10.25338/B87S43>, 2019

960 D'Ambro, E. L., Lee, B. H., Liu, J. M., Shilling, J. E., Gaston, C. J., Lopez-Hilfiker, F. D., Schobesberger,  
961 S., Zaveri, R. A., Mohr, C., Lutz, A., Zhang, Z. F., Gold, A., Surratt, J. D., Rivera-Rios, J. C., Keutsch,  
962 F. N., and Thornton, J. A.: Molecular composition and volatility of isoprene photochemical  
963 oxidation secondary organic aerosol under low- and high-NO<sub>x</sub> conditions, *Atmospheric Chemistry  
964 and Physics*, 17, 159-174, <https://doi.org/10.5194/acp-17-159-2017>, 2017.

965 D'Ambro, E. L., Schobesberger, S., Zaveri, R. A., Shilling, J. E., Lee, B. H., Lopez-Hilfiker, F. D., Mohr,  
966 C., and Thornton, J. A.: Isothermal Evaporation of alpha-Pinene Ozonolysis SOA: Volatility, Phase  
967 State, and Oligomeric Composition, *Acs Earth Space Chem*, 2, 1058-1067,  
968 <https://doi.org/10.1021/acsearthspacechem.8b00084>, 2018.

969 D'Ambro, E. L., Schobesberger, S., Gaston, C. J., Lopez-Hilfiker, F. D., Lee, B. H., Liu, J., Zelenyuk,  
970 A., Bell, D., Cappa, C. D., Helgestad, T., Li, Z., Guenther, A., Wang, J., Wise, M., Caylor, R., Surratt,  
971 J. D., Riedel, T., Hyttinen, N., Salo, V. T., Hasan, G., Kurtén, T., Shilling, J. E., and Thornton, J. A.:  
972 Chamber-based insights into the factors controlling IEPOX SOA yield, composition, and volatility,  
973 *Atmos. Chem. Phys. Discuss.*, 2019, 1-20, <https://doi.org/10.5194/acp-2019-271>, 2019.

974 Faxon, C., Hammes, J., Le Breton, M., Pathak, R. K., and Hallquist, M.: Characterization of organic  
975 nitrate constituents of secondary organic aerosol (SOA) from nitrate-radical-initiated oxidation  
976 of limonene using high-resolution chemical ionization mass spectrometry, *Atmospheric  
977 Chemistry and Physics*, 18, 5467-5481, <https://doi.org/10.5194/acp-18-5467-2018>, 2018.

978 Gaston, C. J., Quinn, P. K., Bates, T. S., Gilman, J. B., Bon, D. M., Kuster, W. C., and Prather, K. A.:  
979 The impact of shipping, agricultural, and urban emissions on single particle chemistry observed  
980 aboard the R/V Atlantis during CalNex, *J Geophys Res-Atmos*, 118, 5003-5017,  
981 <https://doi.org/10.1002/jgrd.50427>, 2013.

982 Gaston, C. J., Lopez-Hilfiker, F. D., Whybrew, L. E., Hadley, O., McNair, F., Gao, H. L., Jaffe, D. A.,  
983 and Thornton, J. A.: Online molecular characterization of fine particulate matter in Port Angeles,  
984 WA: Evidence for a major impact from residential wood smoke, *Atmos Environ*, 138, 99-107,  
985 <https://doi.org/10.1016/j.atmosenv.2016.05.013>, 2016.

986 Giorio, C., Tapparo, A., Dall'Osto, M., Harrison, R. M., Beddows, D. C. S., Di Marco, C., and Nemitz,  
987 E.: Comparison of three techniques for analysis of data from an Aerosol Time-of-Flight Mass  
988 Spectrometer, *Atmos Environ*, 61, 316-326, <https://doi.org/10.1016/j.atmosenv.2012.07.054>,  
989 2012.

990 Goldstein, A. H., and Galbally, I. E.: Known and unexplored organic constituents in the earth's  
991 atmosphere, *Environ Sci Technol*, 41, 1514-1521, <https://doi.org/10.1021/es072476p>, 2007.

992 Gonzalez, T. F.: Clustering to Minimize the Maximum Intercluster Distance, *Theor Comput Sci*, 38,  
993 293-306, [https://doi.org/10.1016/0304-3975\(85\)90224-5](https://doi.org/10.1016/0304-3975(85)90224-5), 1985.

994 Hamilton, J. F., Webb, P. J., Lewis, A. C., Hopkins, J. R., Smith, S., and Davy, P.: Partially oxidised  
995 organic components in urban aerosol using GCXGC-TOF/MS, *Atmospheric Chemistry and Physics*,  
996 4, 1279-1290, <https://doi.org/10.5194/acp-4-1279-2004>, 2004.

997 Huang, W., Saathoff, H., Pajunoja, A., Shen, X. L., Naumann, K. H., Wagner, R., Virtanen, A., Leisner,  
998 T., and Mohr, C.: alpha-Pinene secondary organic aerosol at low temperature: chemical

999 composition and implications for particle viscosity, *Atmospheric Chemistry and Physics*, 18, 2883-  
1000 2898, <https://doi.org/10.5194/acp-18-2883-2018>, 2018.

1001 Isaacman-VanWertz, G., Massoli, P., O'Brien, R. E., Nowak, J. B., Canagaratna, M. R., Jayne, J. T.,  
1002 Worsnop, D. R., Su, L., Knopf, D. A., Misztal, P. K., Arata, C., Goldstein, A. H., and Kroll, J. H.: Using  
1003 advanced mass spectrometry techniques to fully characterize atmospheric organic carbon:  
1004 current capabilities and remaining gaps, *Faraday Discussions*, 200, 579-598,  
1005 <https://doi.org/10.1039/c7fd00021a>, 2017.

1006 Joo, T., Rivera-Rios, J. C., Takeuchi, M., Alvarado, M. J., and Ng, N. L.: Secondary Organic Aerosol  
1007 Formation from Reaction of 3-Methylfuran with Nitrate Radicals, *Acs Earth Space Chem*,  
1008 <https://doi.org/10.1021/acsearthspacechem.9b00068>, 2019.

1009 Kirchner, U., Vogt, R., Natzeck, C., and Goschnick, J.: Single particle MS, SNMS, SIMS, XPS, and  
1010 FTIR spectroscopic analysis of soot particles during the AIDA campaign, *Journal of Aerosol Science*,  
1011 34, 1323-1346, [https://doi.org/10.1016/S0021-8502\(03\)00362-8](https://doi.org/10.1016/S0021-8502(03)00362-8), 2003.

1012 Le Breton, M., Psichoudaki, M., Hallquist, M., Watne, A. K., Lutz, A., and Hallquist, A. M.:  
1013 Application of a FIGAERO ToF CIMS for on-line characterization of real-world fresh and aged  
1014 particle emissions from buses, *Aerosol Science and Technology*, 53, 244-259,  
1015 <https://doi.org/10.1080/02786826.2019.1566592>, 2019.

1016 Lee, A. K. Y., Willis, M. D., Healy, R. M., Onasch, T. B., and Abbatt, J. P. D.: Mixing state of  
1017 carbonaceous aerosol in an urban environment: single particle characterization using the soot  
1018 particle aerosol mass spectrometer (SP-AMS), *Atmospheric Chemistry and Physics*, 15, 1823-  
1019 1841, <https://doi.org/10.5194/acp-15-1823-2015>, 2015.

1020 Lee, B., Lopez-Hilfiker, F. D., D'Ambro, E. L., Zhou, P. T., Boy, M., Petaja, T., Hao, L. Q., Virtanen,  
1021 A., and Thornton, J. A.: Semi-volatile and highly oxygenated gaseous and particulate organic  
1022 compounds observed above a boreal forest canopy, *Atmospheric Chemistry and Physics*, 18,  
1023 11547-11562, <https://doi.org/10.5194/acp-18-11547-2018>, 2018.

1024 Lee, B. H., Lopez-Hilfiker, F. D., Mohr, C., Kurten, T., Worsnop, D. R., and Thornton, J. A.: An Iodide-  
1025 Adduct High-Resolution Time-of-Flight Chemical-Ionization Mass Spectrometer: Application to  
1026 Atmospheric Inorganic and Organic Compounds, *Environ Sci Technol*, 48, 6309-6317,  
1027 <https://doi.org/10.1021/es500362a>, 2014.

1028 Lee, B. H., Mohr, C., Lopez-Hilfiker, F. D., Lutz, A., Hallquist, M., Lee, L., Romer, P., Cohen, R. C.,  
1029 Iyer, S., Kurten, T., Hu, W. W., Day, D. A., Campuzano-Jost, P., Jimenez, J. L., Xu, L., Ng, N. L., Guo,  
1030 H. Y., Weber, R. J., Wild, R. J., Brown, S. S., Koss, A., de Gouw, J., Olson, K., Goldstein, A. H., Seco,  
1031 R., Kim, S., McAvey, K., Shepson, P. B., Starn, T., Baumann, K., Edgerton, E. S., Liu, J. M., Shilling,  
1032 J. E., Miller, D. O., Brune, W., Schobesberger, S., D'Ambro, E. L., and Thornton, J. A.: Highly  
1033 functionalized organic nitrates in the southeast United States: Contribution to secondary organic  
1034 aerosol and reactive nitrogen budgets, *P Natl Acad Sci USA*, 113, 1516-1521,  
1035 <https://doi.org/10.1073/pnas.1508108113>, 2016.

1036 Li, Z., and Cappa, C. D.: Noise Sorted Scanning Clustering Algorithm (Version v1.0.3), Zenodo,  
1037 <https://doi.org/10.5281/zenodo.3361797>, 2019

1038 Liu, J. M., D'Ambro, E. L., Lee, B. H., Lopez-Hilfiker, F. D., Zaveri, R. A., Rivera-Rios, J. C., Keutsch,  
1039 F. N., Iyer, S., Kurten, T., Zhang, Z. F., Gold, A., Surratt, J. D., Shilling, J. E., and Thornton, J. A.:  
1040 Efficient Isoprene Secondary Organic Aerosol Formation from a Non-IEPDX Pathway, *Environ Sci  
1041 Technol*, 50, 9872-9880, <https://doi.org/10.1021/acs.est.6b01872>, 2016.

1042 Liu, S., Shilling, J. E., Song, C., Hiranuma, N., Zaveri, R. A., and Russell, L. M.: Hydrolysis of  
1043 Organonitrate Functional Groups in Aerosol Particles, *Aerosol Science and Technology*, 46, 1359-  
1044 1369, <https://doi.org/10.1080/02786826.2012.716175>, 2012.

1045 Liu, S., Russell, L. M., Sueper, D. T., and Onasch, T. B.: Organic particle types by single-particle  
1046 measurements using a time-of-flight aerosol mass spectrometer coupled with a light scattering  
1047 module, *Atmospheric Measurement Techniques*, 6, 187-197, [https://doi.org/10.5194/amt-6-](https://doi.org/10.5194/amt-6-187-2013)  
1048 [187-2013](https://doi.org/10.5194/amt-6-187-2013), 2013.

1049 Lopez-Hilfiker, F. D., Mohr, C., Ehn, M., Rubach, F., Kleist, E., Wildt, J., Mentel, T. F., Lutz, A.,  
1050 Hallquist, M., Worsnop, D., and Thornton, J. A.: A novel method for online analysis of gas and  
1051 particle composition: description and evaluation of a Filter Inlet for Gases and AEROSols  
1052 (FIGAERO), *Atmospheric Measurement Techniques*, 7, 983-1001, [https://doi.org/10.5194/amt-](https://doi.org/10.5194/amt-7-983-2014)  
1053 [7-983-2014](https://doi.org/10.5194/amt-7-983-2014), 2014.

1054 Lopez-Hilfiker, F. D., Mohr, C., Ehn, M., Rubach, F., Kleist, E., Wildt, J., Mentel, T. F., Carrasquillo,  
1055 A. J., Daumit, K. E., Hunter, J. F., Kroll, J. H., Worsnop, D. R., and Thornton, J. A.: Phase partitioning  
1056 and volatility of secondary organic aerosol components formed from  $\alpha$ -pinene ozonolysis and OH  
1057 oxidation: the importance of accretion products and other low volatility compounds,  
1058 *Atmospheric Chemistry and Physics*, 15, 7765-7776, <https://doi.org/10.5194/acp-15-7765-2015>,  
1059 2015.

1060 Lopez-Hilfiker, F. D., Mohr, C., D'Ambro, E. L., Lutz, A., Riedel, T. P., Gaston, C. J., Iyer, S., Zhang,  
1061 Z., Gold, A., Surratt, J. D., Lee, B. H., Kurten, T., Hu, W. W., Jimenez, J., Hallquist, M., and Thornton,  
1062 J. A.: Molecular Composition and Volatility of Organic Aerosol in the Southeastern U.S.:  
1063 Implications for IEPOX Derived SOA, *Environ Sci Technol*, 50, 2200-2209,  
1064 <https://doi.org/10.1021/acs.est.5b04769>, 2016.

1065 Mohr, C., Lopez-Hilfiker, F. D., Yli-Juuti, T., Heitto, A., Lutz, A., Hallquist, M., D'Ambro, E. L.,  
1066 Rissanen, M. P., Hao, L. Q., Schobesberger, S., Kulmala, M., Mauldin, R. L., Makkonen, U., Sipila,  
1067 M., Petaja, T., and Thornton, J. A.: Ambient observations of dimers from terpene oxidation in the  
1068 gas phase: Implications for new particle formation and growth, *Geophysical Research Letters*, 44,  
1069 2958-2966, <https://doi.org/10.1002/2017gl072718>, 2017.

1070 Murphy, D. M., Middlebrook, A. M., and Warshawsky, M.: Cluster analysis of data from the  
1071 Particle Analysis by Laser Mass Spectrometry (PALMS) instrument, *Aerosol Science and*  
1072 *Technology*, 37, 382-391, <https://doi.org/10.1080/02786820300971>, 2003.

1073 Pinero-Garcia, F., Ferro-Garcia, M. A., Chham, E., Cobos-Diaz, M., and Gonzalez-Rodelas, P.: A  
1074 cluster analysis of back trajectories to study the behaviour of radioactive aerosols in the south-  
1075 east of Spain, *J Environ Radioactiv*, 147, 142-152, <https://doi.org/10.1016/j.jenvrad.2015.05.029>,  
1076 2015.

1077 Praske, E., Otkjaer, R. V., Crouse, J. D., Hethcox, J. C., Stoltz, B. M., Kjaergaard, H. G., and  
1078 Wennberg, P. O.: Atmospheric autoxidation is increasingly important in urban and suburban  
1079 North America, *P Natl Acad Sci USA*, 115, 64-69, <https://doi.org/10.1073/pnas.1715540115>, 2018.

1080 Rebotier, T. P., and Prather, K. A.: Aerosol time-of-flight mass spectrometry data analysis: A  
1081 benchmark of clustering algorithms, *Anal Chim Acta*, 585, 38-54,  
1082 <https://doi.org/10.1016/j.aca.2006.12.009>, 2007.

1083 Reitz, P., Zorn, S. R., Trimborn, S. H., and Trimborn, A. M.: A new, powerful technique to analyze  
1084 single particle aerosol mass spectra using a combination of OPTICS and the fuzzy c-means

1085 algorithm, *Journal of Aerosol Science*, 98, 1-14, <https://doi.org/10.1016/j.jaerosci.2016.04.003>,  
1086 2016.

1087 Roth, A., Schneider, J., Klimach, T., Mertes, S., van Pinxteren, D., Herrmann, H., and Borrmann, S.:  
1088 Aerosol properties, source identification, and cloud processing in orographic clouds measured by  
1089 single particle mass spectrometry on a central European mountain site during HCCT-2010,  
1090 *Atmospheric Chemistry and Physics*, 16, 505-524, <https://doi.org/10.5194/acp-16-505-2016>,  
1091 2016.

1092 Schobesberger, S., D'Ambro, E. L., Lopez-Hilfiker, F. D., Mohr, C., and Thornton, J. A.: A model  
1093 framework to retrieve thermodynamic and kinetic properties of organic aerosol from  
1094 composition-resolved thermal desorption measurements, *Atmospheric Chemistry and Physics*,  
1095 18, 14757-14785, <https://doi.org/10.5194/acp-18-14757-2018>, 2018.

1096 Song, X. H., Hopke, P. K., Fergenson, D. P., and Prather, K. A.: Classification of single particles  
1097 analyzed by ATOFMS using an artificial neural network, *ART-2A, Anal Chem*, 71, 860-865,  
1098 <https://doi.org/10.1021/ac9809682>, 1999.

1099 Stolzenburg, D., Fischer, L., Vogel, A. L., Heinritzi, M., Schervish, M., Simon, M., Wagner, A. C.,  
1100 Dada, L., Ahonen, L. R., Amorim, A., Baccarini, A., Bauer, P. S., Baumgartner, B., Bergen, A., Bianchi,  
1101 F., Breitenlechner, M., Brilke, S., Mazon, S. B., Chen, D. X., Dias, A., Draper, D. C., Duplissy, J.,  
1102 Haddad, I., Finkenzeller, H., Frege, C., Fuchs, C., Garmash, O., Gordon, H., He, X., Helm, J.,  
1103 Hofbauer, V., Hoyle, C. R., Kim, C., Kirkby, J., Kontkanen, J., Kuerten, A., Lampilahti, J., Lawler, M.,  
1104 Lehtipalo, K., Leiminger, M., Mai, H., Mathot, S., Mentler, B., Molteni, U., Nie, W., Nieminen, T.,  
1105 Nowak, J. B., Ojdanic, A., Onnela, A., Passananti, M., Petaja, T., Quelever, L. L. J., Rissanen, M. P.,  
1106 Sarnela, N., Schallhart, S., Tauber, C., Tome, A., Wagner, R., Wang, M., Weitz, L., Wimmer, D.,  
1107 Xiao, M., Yan, C., Ye, P., Zha, Q., Baltensperger, U., Curtius, J., Dommen, J., Flagan, R. C., Kulmala,  
1108 M., Smith, J. N., Worsnop, D. R., Hansel, A., Donahue, N. M., and Winkler, P. M.: Rapid growth  
1109 of organic aerosol nanoparticles over a wide tropospheric temperature range, *P Natl Acad Sci USA*,  
1110 115, 9122-9127, <https://doi.org/10.1073/pnas.1807604115>, 2018.

1111 Takahama, S., Gilardoni, S., Russell, L. M., and Kilcoyne, A. L. D.: Classification of multiple types  
1112 of organic carbon composition in atmospheric particles by scanning transmission X-ray  
1113 microscopy analysis, *Atmos Environ*, 41, 9435-9451,  
1114 <https://doi.org/10.1016/j.atmosenv.2007.08.051>, 2007.

1115 Wang, D. S., and Ruiz, L. H.: Chlorine-initiated oxidation of n-alkanes under high-NO<sub>x</sub> conditions:  
1116 insights into secondary organic aerosol composition and volatility using a FIGAERO-CIMS,  
1117 *Atmospheric Chemistry and Physics*, 18, 15535-15553, [https://doi.org/10.5194/acp-18-15535-](https://doi.org/10.5194/acp-18-15535-2018)  
1118 [2018](https://doi.org/10.5194/acp-18-15535-2018), 2018.

1119 Wegner, T., Hussein, T., Hameri, K., Vesala, T., Kulmala, M., and Weber, S.: Properties of aerosol  
1120 signature size distributions in the urban environment as derived by cluster analysis, *Atmos*  
1121 *Environ*, 61, 350-360, <https://doi.org/10.1016/j.atmosenv.2012.07.048>, 2012.

1122 Zhao, W. X., Hopke, P. K., and Prather, K. A.: Comparison of two cluster analysis methods using  
1123 single particle mass spectra, *Atmos Environ*, 42, 881-892,  
1124 <https://doi.org/10.1016/j.atmosenv.2007.10.024>, 2008.

1125 Zhao, Y., Thornton, J. A., and Pye, H. O. T.: Quantitative constraints on autoxidation and dimer  
1126 formation from direct probing of monoterpene-derived peroxy radical chemistry, *P Natl Acad Sci*  
1127 *USA*, 115, 12142-12147, <https://doi.org/10.1073/pnas.1812147115>, 2018.

1128 Zhou, L. M., Hopke, P. K., and Venkatachari, P.: Cluster analysis of single particle mass spectra  
1129 measured at Flushing, NY, Anal Chim Acta, 555, 47-56, <https://doi.org/10.1016/j.aca.2005.08.061>,  
1130 2006.  
1131

1132

1133 **10. Tables**1134 **Table 1.** Details of SOA formation and chamber conditions for all the example SOA systems.

Exp #	Precursor		Oxidant		Seeds		UV	T (°C)	RH (%)	NO <sup>#5</sup> (ppb)	M <sub>p</sub> <sup>#&amp;</sup> (µg/m <sup>3</sup> )	FIGAERO Operation <sub>s</sub>
	Type	Conc. <sup>#</sup> (ppb)	Type	Conc. <sup>##</sup> (ppm)	Type	D <sub>p</sub> <sup>##</sup> (nm)						
1*	α-pinene	10	OH (H <sub>2</sub> O <sub>2</sub> )	1.0	AS <sup>&amp;</sup>	50	On	25	50	-	5.1	Normal
2	Δ-3-carene	10	OH (H <sub>2</sub> O <sub>2</sub> )	0.25	AS	50	On	25	50	-	5.2	Normal
3a	α-pinene	10	OH (H <sub>2</sub> O <sub>2</sub> )	1.0	AS	50	On	25	50	5	8.3	Normal
3b										10	9.2	
3c										25	9.1	
4a	α-pinene	10	O <sub>3</sub>	0.1	PS <sup>&amp;&amp;</sup>	50	Off	25	80	-	4.0	Normal
4b												1 h wait
4c												3 h wait
4d												6 h wait
4e												24 h wait

\* Experiment #1 is a case study used to test the performances of different clustering algorithms

# Conc. of precursors are the concentrations expected in the chamber with the absence of any chemistry

## For OH, conc. refers to concentration of H<sub>2</sub>O<sub>2</sub> injected into the chamber; for O<sub>3</sub>, conc. refers to steady-state concentration of O<sub>3</sub> in the chamber during SOA formation

## Seed particles are size-selected in all the experiments

#5 NO concentration refers to the targeted NO concentration when NO is injected into the chamber. The actual steady-state concentration of NO is lower than targeted. "-" indicates that no external NO is added to the chamber

#& M<sub>p</sub> is the estimated mass concentration of particles including SOA and seeds measured by SMPS when the chamber is at steady-state, except for experiment 4 where M<sub>p</sub> is the mass concentration of SOA only

<sup>s</sup> Normal operation mode means the desorption process starts immediately after collection period. X h wait means that particles are isothermally diluted for X hours before the desorption process is initiated

& AS = ammonium sulfate

&& PS = potassium sulfate

1135

1136

1137

**Table 2.** Comparison of different clustering algorithms

Clustering Algorithms	k-means	k-medoids	Mean-shift	DBSCAN	FPClustering	NSSC
Assign all the members?	Yes	Yes	No	No	Yes	No
Identify single-member clusters?	No	No	Yes	No	No	Yes
Robust solution?	No	No	No	Yes	No	Yes
Controlled distance from the center of clusters?	No	No	Yes	No	No	Yes
Influence of noise?	large	large	small	small	large	Small
Key preset parameters	$N_c$	$N_c$	$\varepsilon, N_{min}$	$\varepsilon$	Initial seed	$\varepsilon, N_{min}$
Software used in this study	Igor	R	Python	Igor	Igor	Igor

1138  
1139



1140 **Table 3.** Parameters and thresholds used for the data processing and noise-sorted scanning clustering for  
 1141 all the example experiments.

Expt #	SOA type	Pre-processing						Clustering				
		$N_{total}$	$N_{anomalous}$	$N_{filtered}$	$f_{m,filtered}$	$\zeta_{ref}$	$f_{m,ref}$	$\varepsilon$	$N_c$	$N_{c,one}$	$f_{m,unclustered}$	$R_{interCist}$
1	$\alpha$ -pinene + OH	298	4	188	7.5	0.021	0.67	2.6	11	0	0.00	2.01
2	$\Delta$ -3-carene + OH	298	5	183	9.3	0.019	0.57	2.1	9	1	0.27	2.36
3a	$\alpha$ -pinene + OH + NO	Single	6	204	15.3	0.025	0.55	2.2	9	1	1.52	2.06
3b			6	204	17.5	-	-	-	9	1	1.72	-
3c			6	204	21.0	-	-	-	9	1	2.27	-
3a		Multi	2	208	15.5	0.025	0.55	2.2	9	1	1.52	2.06
3b			3	195	12.6	0.027	0.54	2.3	10	1	1.29	2.10
3c			6	200	12.8	0.028	0.43	2.5	12	1	1.21	1.96
4a	$\alpha$ -pinene + O <sub>3</sub>	Single	10	185	11.5	0.025	0.42	2.2	10	2	0.67	2.28
4b			10	185	14.0	-	-	-	10	2	0.79	-
4c			10	185	14.0	-	-	-	10	2	0.84	-
4d		10	185	13.8	-	-	-	10	2	0.83	-	
4e		10	185	17.6	-	-	-	10	2	0.82	-	
4a		Multi	1	191	11.4	0.025	0.41	2.2	11	2	1.04	2.22
4b	0		210	16.5	0.044	0.41	3.3	8	4	0.00	2.02	
4c	5		205	14.3	0.048	0.42	3.1	9	2	1.06	1.66	
4d	3		203	12.8	0.055	0.39	3.3	8	1	2.50	1.80	
4e	3		213	16.1	0.053	0.41	3.4	7	2	0.98	1.97	

$N_{total}$  – Total number of ions characterized by CIMS

$N_{anomalous}$  – Number of anomalous ions

$N_{filtered}$  – Number of ions filtered out from the following clustering due to high levels of noises

$f_{m,filtered}$  – Mass fraction of the ions filtered out due to high levels of noises, expressed in %

$\zeta_{ref}$  – Noise threshold. Ions with noise levels above this threshold are excluded from clustering

$f_{m,ref}$  – The threshold of mass contribution (%) to identify an ion as significant

$\varepsilon$  – distance criterion

$N_c$  – Number of clusters determined with two or more members

$N_{c,one}$  – Number of clusters determined with only one member

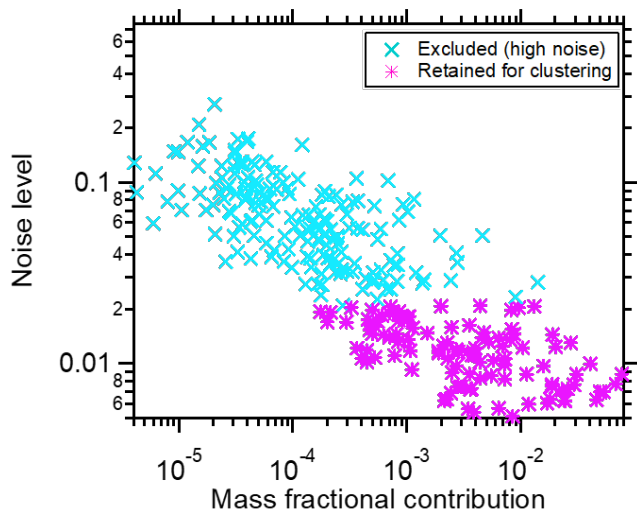
$f_{m,unclustered}$  – Mass fraction of unclustered ions, expressed in %

$R_{interCist}$  – The ratio of the average inter-cluster distance over the distance criterion  $\varepsilon$

1142

1143

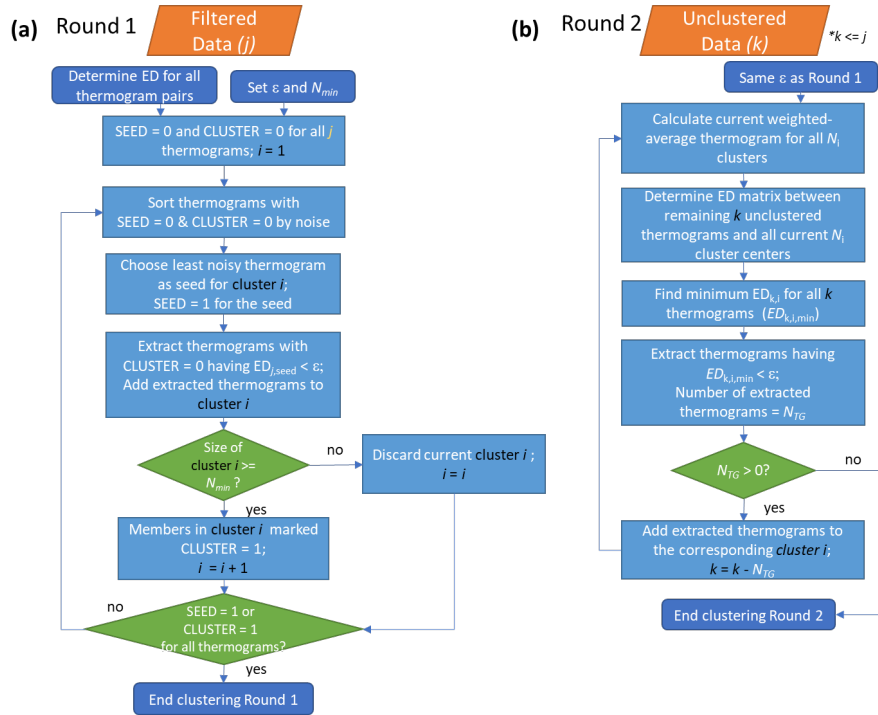
1144 **11. Figures**



1145

1146 **Figure 1:** The relationship between thermogram noise levels and the fractional contributions of the  
1147 corresponding ions to total mass, for  $\alpha$ -pinene + OH SOA. The noise threshold,  $\xi_{ref} = 0.021$  and is used to  
1148 distinguish high-noise thermograms (cyan markers) from thermograms having acceptable noise levels  
1149 (pink markers).

1150

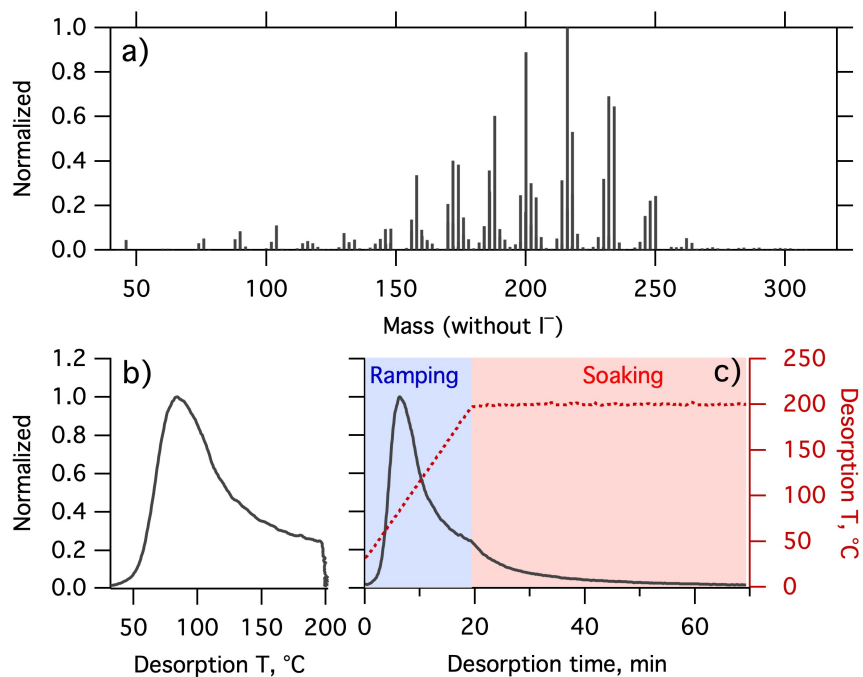


1151

1152 **Figure 2:** Flow of the noise-sorted scanning clustering. There are two rounds of clustering. (a) Round 1:  
 1153 The ED between all thermogram pairs are calculated and two parameters,  $\epsilon$  and  $N_{min}$ , are set. Each  
 1154 thermogram is initialized with state SEED = 0 and CLUSTER = 0. Only thermograms with SEED = 0 and  
 1155 CLUSTER = 0 can serve as seeds, while thermograms with CLUSTER = 0 can be added to new clusters. The  
 1156 procedure terminates when all the thermograms are marked either SEED = 1 or CLUSTER = 1. (b) Round  
 1157 2: Seeds are specified as the weighted-average thermogram for each cluster, and any remaining  
 1158 unclustered thermograms from Round 1 are potentially added to these clusters. With the indexing,  $j$  refers  
 1159 to the total number of thermograms,  $i$  to the number of clusters, and  $k$  to the number of unclustered  
 1160 thermograms after Round 1.

1161

1162

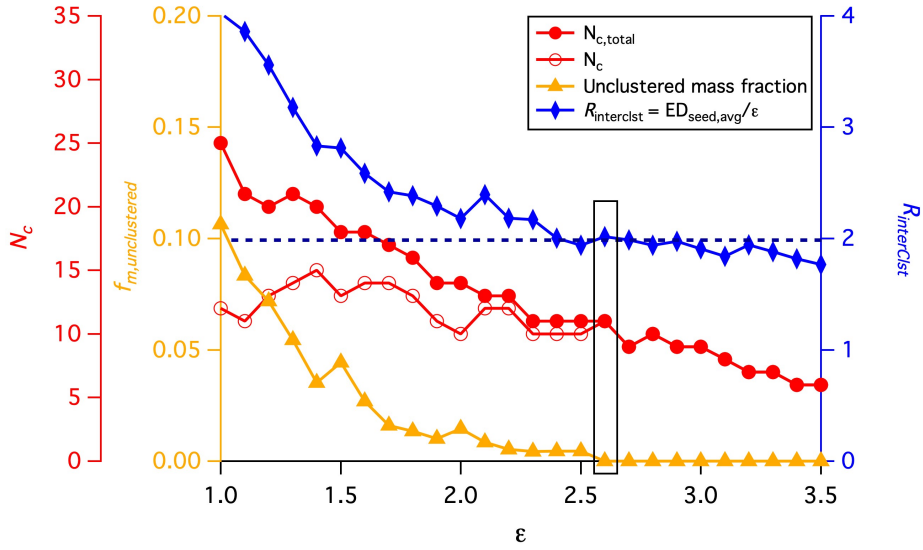


1163  
1164

1165 **Figure 3.** (a) Mass spectrum of  $\alpha$ -pinene + OH SOA measured by FIGAERO-CIMS. The mass excludes iodine.  
1166 (b) Normalized thermogram of the bulk SOA versus temperature. (c) Normalized thermogram of the bulk  
1167 SOA versus time (black line) and the variation in desorption temperature with time (dark red dashed line).  
1168 The long tail during the soaking period is evident when the thermogram is considered in time space. The  
1169 light blue shaded area denotes the ramping period and the pink shaded area the soaking period.

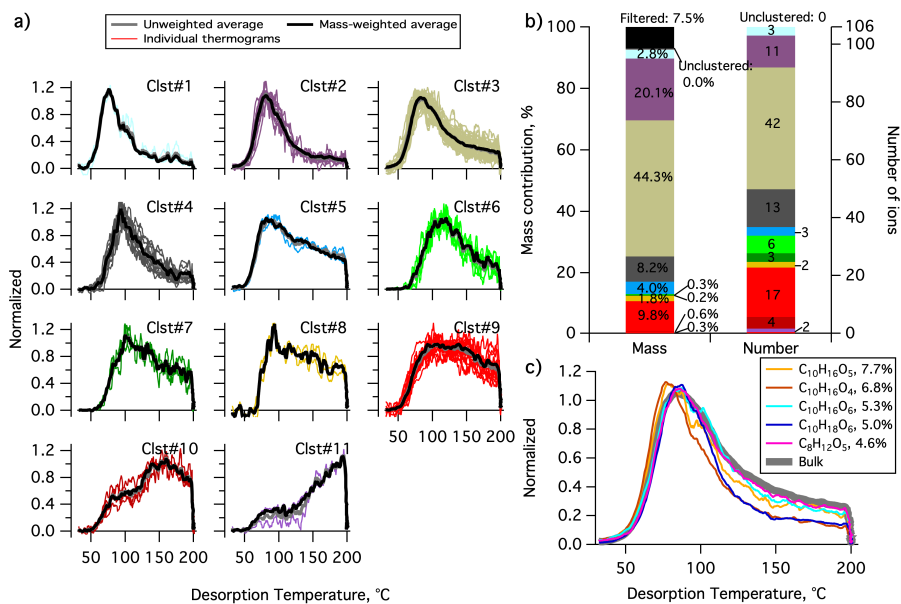
1170

1171



1172  
1173  
1174  
1175  
1176

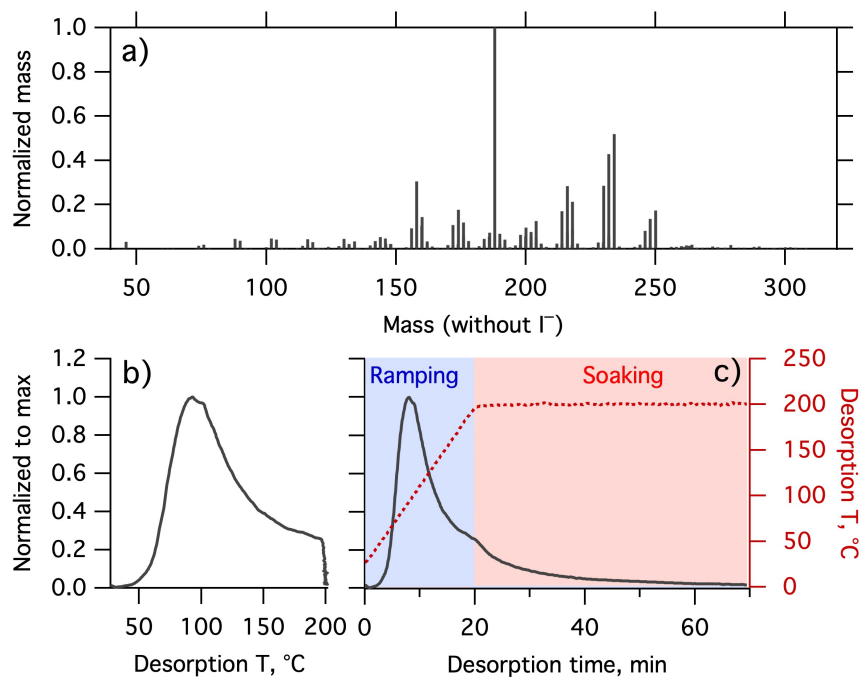
**Figure 4.** The variation of four parameters,  $N_c$ ,  $N_{c,total}$ ,  $f_{m,unclustered}$  and  $R_{interCist}$  as a function of the distance criterion  $\epsilon$ . The black horizontal dashed line guides the judgement for  $R_{interCist} \geq 2$ . The values highlighted by a rectangle are the values corresponding to the optimal  $\epsilon$  used for the clustering analysis.



1177  
 1178 **Figure 5.** Clustering results for  $\alpha$ -pinene + OH SOA. (a) Unweighted average thermograms (bold grey lines),  
 1179 mass-weighted average thermograms (bold black lines) and individual members (colored lines) of the 11  
 1180 clusters identified. (b) Percentage contribution of each cluster to the total mass, as well as the filtered out  
 1181 and unclustered mass percentage (left bar), and the number of ions in each cluster and the unclustered  
 1182 number of ions (right bar). (c) Thermograms of the top 5 ions in terms of mass contribution. The cluster  
 1183 colors are consistent between (a) and (b).

1184

1185



1186

1187

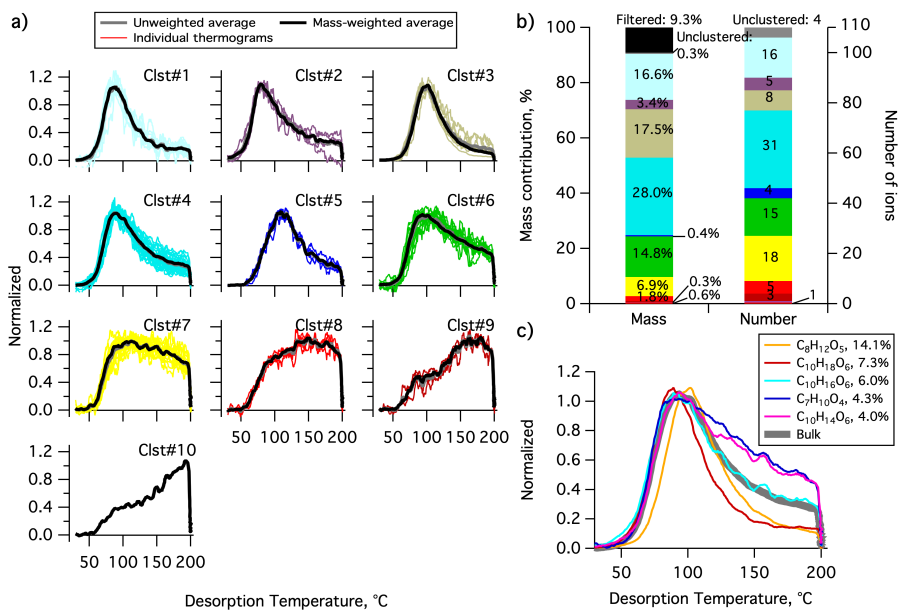
1188

1189

1190

1191

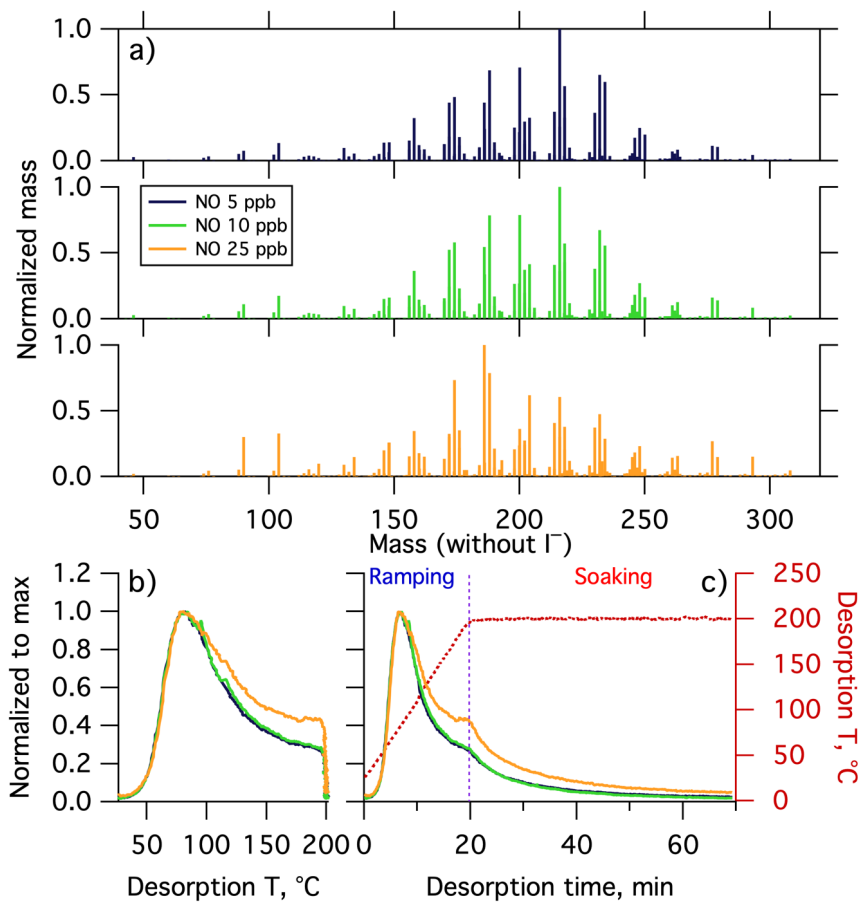
**Figure 6.** Same as Figure 3, but for  $\Delta$ -3-carene + OH SOA. (a) SOA mass spectrum measured by FIGAERO-CIMS. The mass excludes iodine. The normalized thermogram of the bulk SOA versus (b) temperature and (c) time. In (c) the light blue shaded area denotes the ramping period and the pink shaded area the soaking period.



1192 **Figure 7.** Same as Figure 5, but for  $\Delta$ -3-carene + OH SOA. (a) Unweighted average thermograms (bold grey  
 1193 lines), mass-weighted average thermograms (bold black lines) and individual members (colored lines) of  
 1194 the ten clusters identified. (b) Percentage contribution of each cluster to the total mass, as well as the  
 1195 filtered out and unclustered mass percentage (left bar) and number of ions in each cluster and the  
 1196 unclustered number of ions (right bar). (c) Thermograms of the top 5 ions in terms of mass contribution.  
 1197 The cluster colors are consistent between (a) and (b).  
 1198

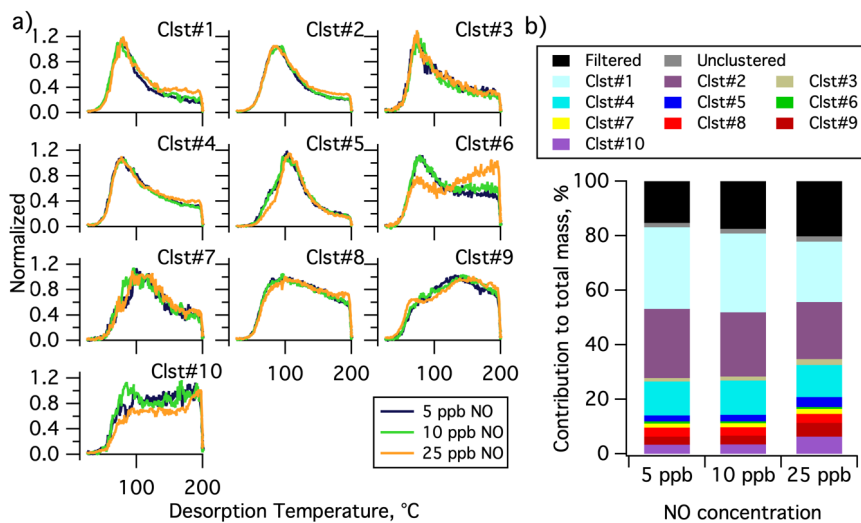
1199





1200 **Figure 8.** (a) Mass spectra of  $\alpha$ -pinene + OH SOA formed with different NO concentrations, normalized to  
 1201 the most abundant ions mass concentration. The mass excludes iodine. Normalized thermograms of the  
 1202 bulk SOA versus (b) temperature and (c) desorption time, with the desorption temperature shown in dark  
 1203 red dashed line. The vertical purple dashed line delineates between ramping and soaking. In all the panels,  
 1204 colors correspond to the NO concentration (see legend).  
 1205

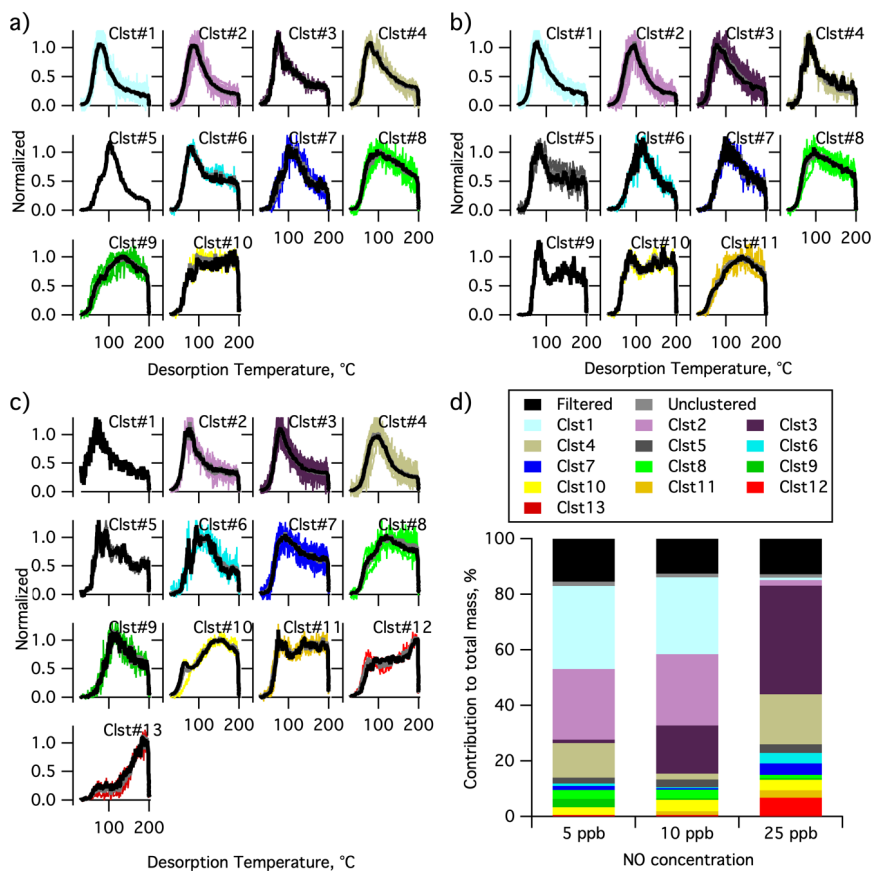
1206



1207

1208 **Figure 9.** Single clustering results for  $\alpha$ -pinene + OH SOA as a function of NO concentration. (a)  
 1209 Comparison of the normalized, weighted average thermograms of the ten clusters for the 5 ppb NO (navy),  
 1210 10 ppb NO (green) and 25 ppb NO (orange) experiments. (b) Contribution of each cluster to the total mass,  
 1211 including the contribution from filtered out ions (black) and unclustered ions (gray). The total mass is  
 1212 calculated independently for each experiment.

1213

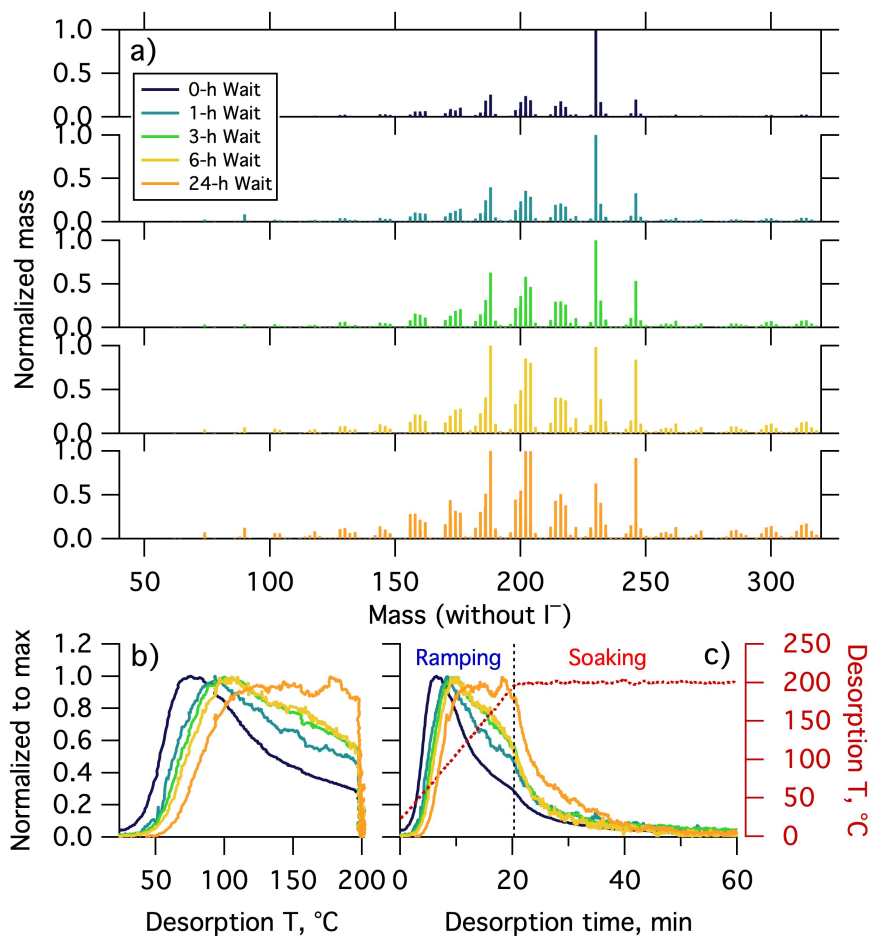


1214

1215 **Figure 10.** Multiple clustering results for  $\alpha$ -pinene + OH SOA as a function of NO concentration. Clustering  
 1216 results are separately shown for the (a) 5 ppb NO, (b) 10 ppb NO, and (c) 25 ppb NO experiments. Each  
 1217 panel includes unweighted average thermograms (grey lines), mass-weighted average thermograms  
 1218 (black lines) and individual cluster members (colored lines). (d) Contribution of each cluster to the total  
 1219 mass for each experiment. The mass contribution of filtered-out ions (black bar) and unclustered ions  
 1220 (grey bar) are also shown.

1221

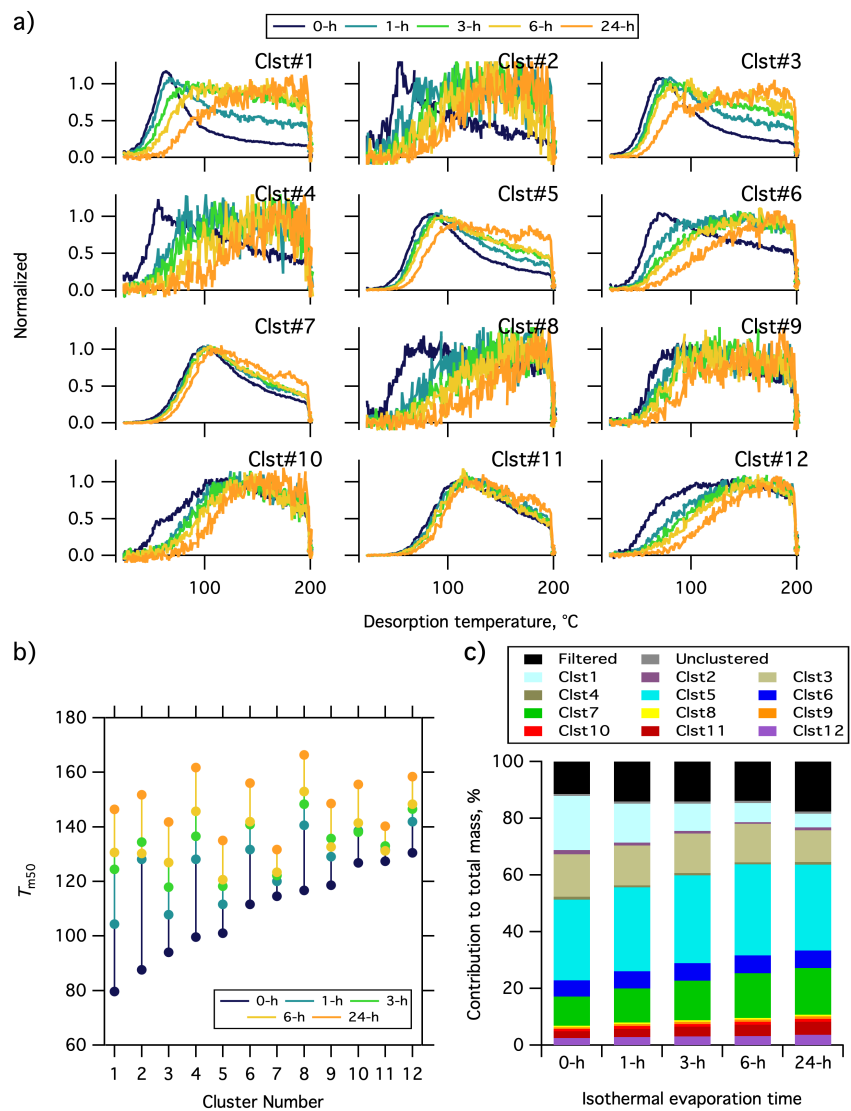
1222



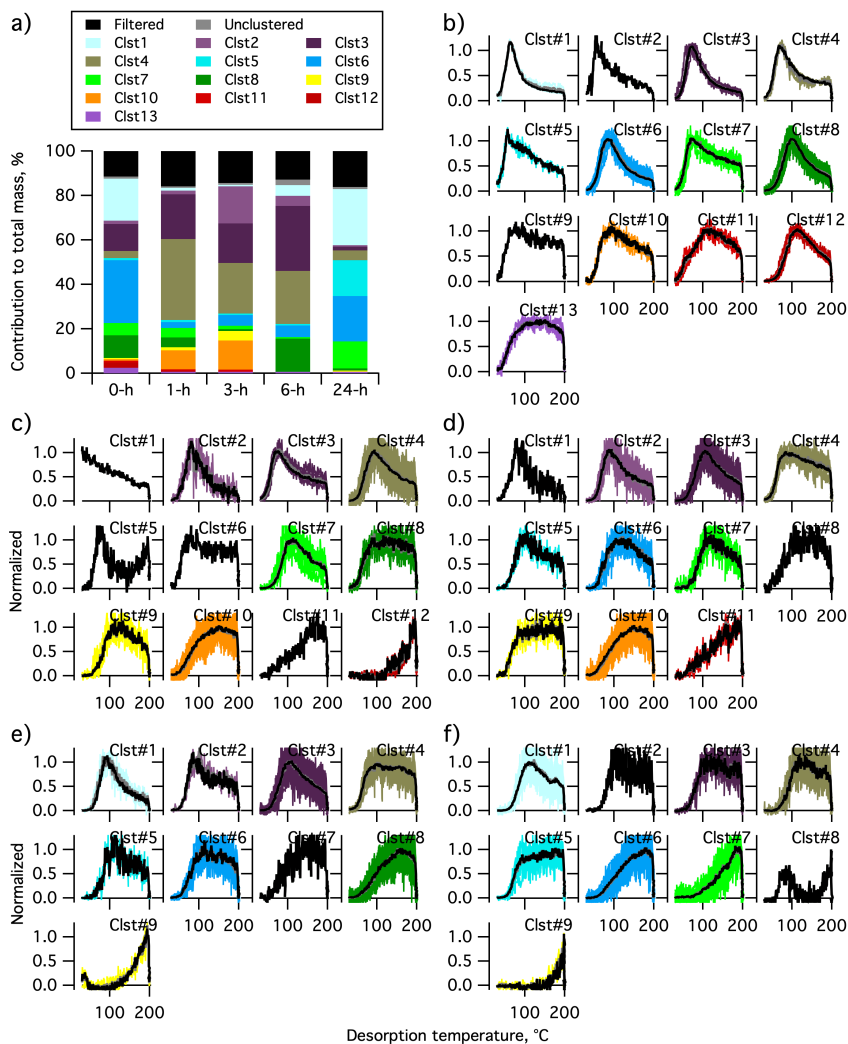
1223

1224 **Figure 11.** (a) Normalized mass spectra of  $\alpha$ -pinene +  $O_3$  SOA measured after different extents of  
1225 isothermal evaporation at room temperature. The mass excludes iodine. The normalized thermograms of  
1226 bulk SOA versus (b) temperature and (c) time, with the desorption temperature shown as a red dashed  
1227 line. The vertical black dashed line in (c) delineates between ramping and soaking. The mass spectrum or  
1228 thermogram colors indicate the isothermal evaporation time (see legend), with darker colors indicating  
1229 shorter times.

1230

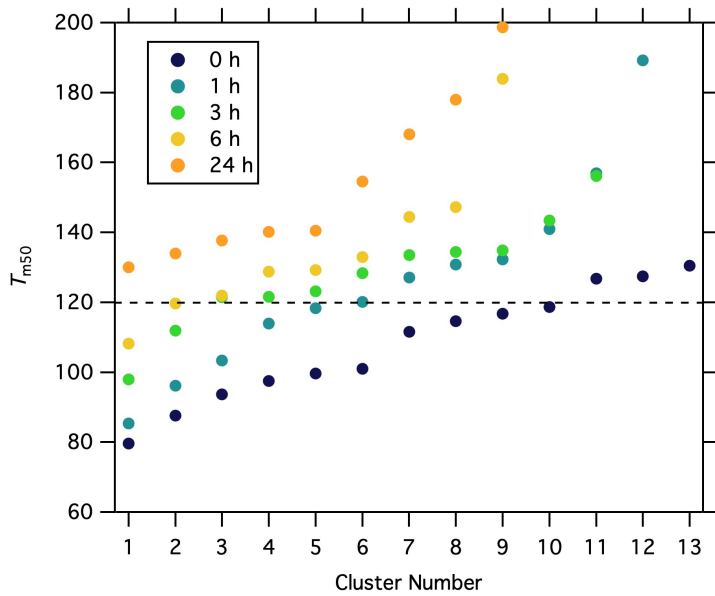


1231  
 1232 **Figure 12.** Single clustering results for  $\alpha$ -pinene +  $O_3$  SOA for different isothermal evaporation times. (a)  
 1233 Comparison of the normalized, weighted-average thermograms of the 12 clusters of 0-h wait (navy), 1-h  
 1234 wait (blue), 3-h wait (green), 6-h wait (yellow) and 24-h wait (orange) experiments. Note that the  
 1235 absolute signals of all of the clusters decrease with evaporation, but to varying extents (Figure S6).



1236  
 1237  
 1238  
 1239  
 1240  
 1241  
 1242

**Figure 13.** Multiple clustering results for  $\alpha$ -pinene +  $O_3$  SOA as a function of isothermal evaporation time. (a) Contribution of each cluster to the total mass for each experiment, along with the contributions of filtered-out ions (black bar) and unclustered ions (gray bar). The number of clusters obtained generally decreases with isothermal evaporation time. (b-f) The unweighted average (gray) and mass-weighted average (black) thermograms, along with the thermograms of individual members of clusters for the (b) 0-h, (c) 1-h, (d) 3-h, (e) 6-h, and (f) 24-h wait experiments. The cluster colors are consistent between panels.



1243

1244 **Figure 14.** The  $T_{m50}$  values of the cluster-specific thermograms from multiple clustering for the five  
 1245 isothermal evaporation experiments.

1246

## Supplemental Material for

### A robust clustering algorithm for analysis of composition-dependent organic aerosol thermal desorption measurements

Ziyue Li<sup>1</sup>, Emma L. D'Ambro<sup>2,3,a</sup>, Siegfried Schobesberger<sup>2,4</sup>, Cassandra J. Gaston<sup>2,b</sup>, Felipe D. Lopez-Hilfiker<sup>2,c</sup>, Jiumeng Liu<sup>5,d</sup>, John E. Shilling<sup>5</sup>, Joel A. Thornton<sup>2,3</sup>, Christopher D. Cappa<sup>1,6</sup>

<sup>1</sup> Atmospheric Science Graduate Group, University of California, Davis, CA, USA

<sup>2</sup> Department of Atmospheric Sciences, University of Washington, Seattle WA, USA

<sup>3</sup> Department of Chemistry, University of Washington, Seattle WA, USA

<sup>4</sup> Department of Applied Physics, University of Eastern Finland, Kuopio, Finland

<sup>5</sup> Atmospheric Sciences and Global Change Division, Pacific Northwest National Laboratory, Richland WA, USA

<sup>6</sup> Department of Civil and Environmental Engineering, University of California, Davis, CA, USA

<sup>a</sup> Oak Ridge Institute for Science and Education, US Environmental Protection Agency, Research Triangle Park, NC, USA

<sup>b</sup> Rosenstiel School of Marine & Atmospheric Science, University of Miami FL, USA

<sup>c</sup> ToFWerk AG, Thun, Switzerland

<sup>d</sup> Now at: School of Environment, Harbin Institute of Technology, Harbin, Heilongjiang, China

The supplemental material includes six tables and six figures, along with additional experimental details for the experiments discussed here

#### ***FIGAERO-CIMS Instrument Description***

The FIGAERO-CIMS instrument has been described previously in detail (Lee et al., 2014; Lopez-Hilfiker et al., 2014). In brief, the measurement of organic aerosol using FIGAERO-CIMS involves two steps: real-time sampling of the gas-phase with simultaneous isothermal collection of particles onto a filter through a separate inlet, followed by temperature programmed thermal desorption and detection of particle-phase species. Thermal desorption of particles occurs in two-stages: a “ramping” and “soaking” period. During ramping, the temperature of UHP N<sub>2</sub> programmatically increases from room temperature to 200 °C, typically at 10 °C min<sup>-1</sup>. The majority of the organic aerosol mass desorbs during the ramping stage. During the soaking period, the UHP N<sub>2</sub> is held at 200 °C for ca. 30–40 mins to facilitate evaporation of the remaining, low-volatility organic mass from the filter.

The desorbed gas-phase compounds are transferred to the high-resolution time-of-flight (HRTof) CIMS for continuous detection and quantification at ca. 1 Hz. Iodide (I<sup>-</sup>) is used as the



reagent ion, which is appropriate for characterization of generally highly oxygenated components comprising most secondary organic aerosol (Isaacman-VanWertz et al., 2017; Lee et al., 2018). In a typical SOA system, hundreds of ions having the general formula  $C_xH_yO_zI^-$  are usually detected. The resulting signal or mass concentration versus temperature (or equivalently time) curves for each ion constitute a thermogram. The overall bulk thermogram is obtained by summing together the individual thermograms.

All individual thermograms are background corrected by subtracting the observed thermograms from appropriate blank experiments. Blank experiments are periodically conducted by placing an additional Teflon filter upstream of the particle filter. The same collection time and desorption processes are used for blank experiments as for samples. The blanks account for contributions from adsorption of gaseous compounds in the air stream and for desorption of compounds from the inner surfaces of the FIGAERO.

#### ***Additional Experimental Details***

Several example applications of the clustering on FIGAERO-CIMS data are discussed in Section 4. These include experiments on SOA derived from: (1) OH +  $\alpha$ -pinene and (2) OH +  $\Delta$ -3-carene, both at low-NO<sub>x</sub> conditions; (3) OH +  $\alpha$ -pinene as a function of [NO]; and (4) O<sub>3</sub> +  $\alpha$ -pinene, but where the SOA is allowed to isothermally evaporate for varying amounts of time prior to thermal desorption. These experiments are briefly described below.

All the experiments were done in a 10.6 m<sup>3</sup> Teflon environmental chamber at Pacific Northwest National Laboratory (PNNL) (Liu et al., 2012; Liu et al., 2016). Details of SOA formation and chamber conditions are summarized in **Table 1**.

Experiments #1-3 were part of the campaign of SOA Formation from Forest Emissions Experiment (SOAFFEE). SOAFFEE was designed and conducted to study the influence of reaction conditions on the formation, composition and properties of biogenic SOA. We consider only a subset of all the SOAFFEE experiments. For the experiments in this study, the chamber operated in continuous-flow mode. The total flow through the chamber was 48.2 L min<sup>-1</sup>, resulting in a residence time of ~3.7 hours. Biogenic precursors were delivered into the chamber by flushing pure air through a glass bulb immersed in a temperature-controlled liquid bath held at 1 °C that

contained a small volume of the pure liquid. OH radicals were produced from the photolysis of H<sub>2</sub>O<sub>2</sub>. An aqueous solution of H<sub>2</sub>O<sub>2</sub> was introduced into a gently warmed glass bulb by a syringe pump. A controlled flow of pure air is passed through the bulb to deliver the desired concentration of H<sub>2</sub>O<sub>2</sub> into the chamber.

Seed particles of (NH<sub>4</sub>)<sub>2</sub>SO<sub>4</sub> were used to enhance SOA formation and reduce losses of semi-volatile reaction products to the chamber walls. Seed particles from atomization were dried and 50 nm particles were selected using a differential mobility analyzer (DMA), which were introduced into the chamber. The chamber relative humidity (RH) was 50%. For experiments #1-2, no NO was added. For experiment #3, a varying amount of NO was added to the chamber via a calibrated gas cylinder and a mass flow controller. A suite of online instruments characterized the chamber outflow, including a UV absorption O<sub>3</sub> analyzer (Thermo Environmental Instruments model 49C), an NO-NO<sub>2</sub>-NO<sub>x</sub> analyzer (Thermo Environmental models 42c and 42i), a TSI scanning mobility particle sizer for the number and volume concentrations of aerosols (SMPS Model 3081), an Ionicon quadrupole proton-transfer-reaction mass spectrometer (PTR-QMS) for concentration of precursors, and an Aerodyne high-resolution time-of-flight mass spectrometer (HR-ToF-AMS) for the submicron particle mass and bulk composition. Additionally, FIGAERO-CIMS was used to monitor the gas- and particle-phase products of VOC oxidation.

Experiment #4 has been described in detail previously (D'Ambro et al., 2018). The work herein focuses on the experiments performed at PNNL at an evaporation RH of 80%. For this set of experiments, FIGAERO-CIMS was operated in two modes, normal and wait mode. In the normal mode, desorption is initiated as soon as sufficient mass is collected. In the wait mode, collected particles were allowed to isothermally evaporate for some period of time prior to thermal desorption. For the isothermal evaporation, the UHP N<sub>2</sub> humidified to 80% RH was continuously passed over the filter at room temperature. Dilution of the air around the filter led to evaporation of SOA. The time of isothermal evaporation ranged from 1 hour to 24 hours, resulting in varying extents of mass loss of SOA from the filter. The chemical compositions of the remaining SOA were then characterized by thermal desorption of the particles.

**Table S1** Chemical characteristics of each cluster identified in the  $\alpha$ -pinene + OH SOA system

Cluster #	Expt. #1 ( $\alpha$ -pinene + OH) Molecular Formula	O:C	H:C	MW	Mass %	# Ions	$T_{m,50}$	$T_{m,75}$	$\Delta T$
1	C <sub>9.3</sub> H <sub>14.9</sub> O <sub>3.3</sub> N <sub>0.0</sub>	0.36	1.60	179.3	2.8	3	86.6	110.7	24.1
2	C <sub>9.6</sub> H <sub>16.6</sub> O <sub>5.1</sub> N <sub>0.0</sub>	0.53	1.72	213.4	20.1	11	93.7	120.6	26.9
3	C <sub>8.5</sub> H <sub>13.0</sub> O <sub>5.1</sub> N <sub>0.0</sub>	0.60	1.54	196.6	44.3	42	103.7	139.2	35.5
4	C <sub>8.2</sub> H <sub>12.9</sub> O <sub>6.7</sub> N <sub>0.0</sub>	0.81	1.56	218.5	8.2	13	110.6	140.8	30.2
5	C <sub>7.4</sub> H <sub>10.8</sub> O <sub>4.0</sub> N <sub>0.0</sub>	0.54	1.46	163.6	4.0	3	116.2	153.1	36.9
6	C <sub>11.1</sub> H <sub>17.8</sub> O <sub>8.1</sub> N <sub>0.0</sub>	0.73	1.60	280.6	0.3	6	126.2	154.5	28.3
7	C <sub>15.3</sub> H <sub>22.6</sub> O <sub>5.4</sub> N <sub>0.0</sub>	0.35	1.48	292.6	0.2	3	129.5	162.4	32.9
8	C <sub>8.5</sub> H <sub>10.9</sub> O <sub>4.0</sub> N <sub>0.0</sub>	0.47	1.29	176.9	1.8	2	131.0	164.1	33.1
9	C <sub>7.2</sub> H <sub>9.4</sub> O <sub>4.5</sub> N <sub>0.0</sub>	0.62	1.31	167.8	9.8	17	131.3	163.7	32.4
10	C <sub>6.9</sub> H <sub>7.9</sub> O <sub>3.5</sub> N <sub>0.0</sub>	0.50	1.15	146.7	0.6	4	145.7	172.1	26.4
11	C <sub>4.1</sub> H <sub>4.0</sub> O <sub>3.9</sub> N <sub>0.0</sub>	0.93	0.97	115.6	0.3	2	161.8	184.2	22.4
Unclustered					0	0			
Filtered					7.5	188			

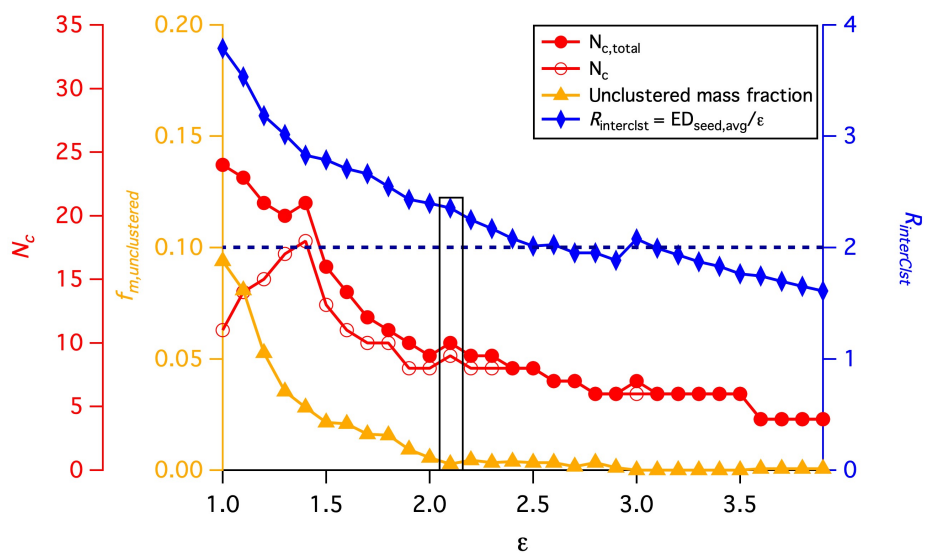


**Figure S1.** Similar to Figure 4, but guidance for determining the optimal  $\epsilon$  for the  $\Delta$ -3-carene +OH SOA. The variation of four parameters,  $N_c$ ,  $N_{c,total}$ ,  $f_{m,unclustered}$  and  $R_{interCist}$  are shown as a function of the distance criterion  $\epsilon$ . The black horizontal dashed line is guide judgement for  $R_{interCist} \geq 2$ . The values highlighted by a rectangle are those corresponding to the optimal  $\epsilon$  used for the following clustering analysis.

**Table S2** Chemical characteristics of each cluster identified in the  $\Delta$ -3-carene + OH SOA system

Cluster #	Expt. #2 ( $\Delta$ -3-carene+ OH) Molecular Formula	O:C	H:C	MW	Mass %	# Ions	$T_{m,50}$	$T_{m,75}$	$\Delta T$
1	C <sub>9.5</sub> H <sub>16.7</sub> O <sub>5.7</sub> N <sub>0.0</sub>	0.60	1.76	221.9	16.6	3	99.4	127.0	27.6
2	C <sub>6.9</sub> H <sub>11.3</sub> O <sub>4.7</sub> N <sub>0.1</sub>	0.68	1.64	170.7	3.4	11	102.3	138.7	36.4
3	C <sub>8.3</sub> H <sub>12.9</sub> O <sub>5.4</sub> N <sub>0.0</sub>	0.65	1.55	198.9	17.5	42	106.9	128.3	21.4
4	C <sub>8.0</sub> H <sub>12.4</sub> O <sub>5.3</sub> N <sub>0.0</sub>	0.65	1.54	193.2	28.0	13	110.1	143.9	33.8
5	C <sub>11.4</sub> H <sub>19.7</sub> O <sub>8.6</sub> N <sub>0.0</sub>	0.76	1.73	294.1	0.4	3	120.1	147.0	26.9
6	C <sub>8.2</sub> H <sub>11.7</sub> O <sub>5.2</sub> N <sub>0.0</sub>	0.63	1.42	193.3	14.8	6	121.4	156.1	34.7
7	C <sub>6.6</sub> H <sub>8.6</sub> O <sub>4.6</sub> N <sub>0.0</sub>	0.69	1.30	161.4	6.9	3	131.3	164.6	33.3
8	C <sub>6.9</sub> H <sub>7.5</sub> O <sub>3.9</sub> N <sub>0.0</sub>	0.56	1.13	153.1	1.8	2	141.4	170.1	28.7
9	C <sub>6.0</sub> H <sub>7.2</sub> O <sub>4.0</sub> N <sub>0.0</sub>	0.68	1.21	143.2	0.3	17	151.2	176.3	25.1
10	C <sub>4.0</sub> H <sub>4.0</sub> O <sub>4.0</sub> N <sub>0.0</sub>	1.00	1.00	116	0.6	4	157.5	181.9	24.4
Unclustered					0.3	4			
Filtered					9.3	183			

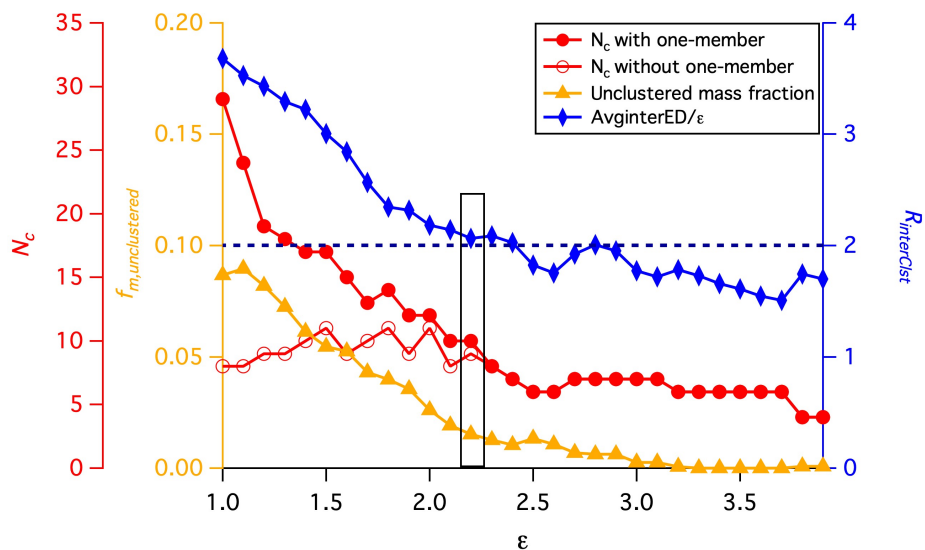


**Figure S2.** Similar to Figure 4, but guidance for determining the optimal  $\epsilon$  for the  $\alpha$ -pinene +OH SOA formed under 5 ppb NO for the single clustering approach. The variation of four parameters,  $N_c$ ,  $N_{c,total}$ ,  $f_{m,unclustered}$  and  $R_{interCist}$  are shown as a function of the distance criterion  $\epsilon$ . The black horizontal dashed line is guide judgement for  $R_{interCist} \geq 2$ . The values highlighted by a rectangle are those corresponding to the optimal  $\epsilon$  used for the following clustering analysis.

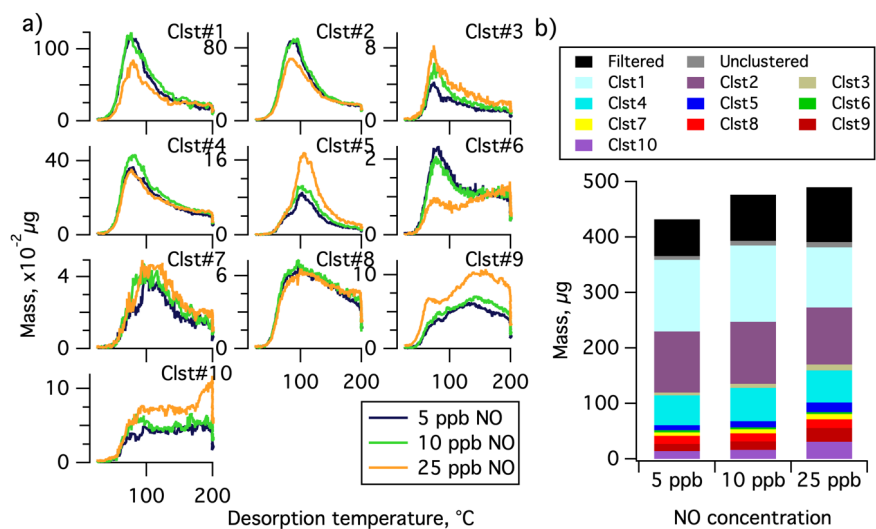


**Figure S3** Similar to **Figure 9** but presented in the absolute sense. (a) Comparison of the summed thermograms of the 10 clusters of 5 ppb (navy), 10 ppb (green) and 25 ppb (orange) NO experiments. (b) Absolute mass of each cluster for each experiment, including the summed mass of filtered out ions (black) and unclustered ions (gray).

**Table S3.** Chemical characteristics of each cluster identified in the  $\alpha$ -pinene + OH + NO SOA system. The single clustering approach is used based on 5 ppb NO experiment.

**Table S3-1.**

Cluster #	Expt. #3 ( $\alpha$ -pinene + OH + NO) Molecular Formula	O:C	H:C	MW	[NO]	[NO]	[NO]	# Ions
					5 ppb	10 ppb	25 ppb	
1	C <sub>8.8</sub> H <sub>14.3</sub> O <sub>4.7</sub> N <sub>0.0</sub>	0.53	1.62	195.1	29.9	28.8	22.1	27
2	C <sub>9.3</sub> H <sub>14.8</sub> O <sub>6.0</sub> N <sub>0.0</sub>	0.65	1.59	222.4	25.4	23.6	20.1	19
3	C <sub>7.5</sub> H <sub>10.7</sub> O <sub>6.4</sub> N <sub>0.4</sub>	0.85	1.42	208.7	1.2	1.4	2.1	2
4	C <sub>8.0</sub> H <sub>11.7</sub> O <sub>4.9</sub> N <sub>0.1</sub>	0.61	1.47	187.5	12.4	12.6	11.9	10
5	C <sub>8.0</sub> H <sub>12.0</sub> O <sub>6.0</sub> N <sub>0.0</sub>	0.75	1.50	204.0	2.2	2.4	3.6	1
6	C <sub>5.5</sub> H <sub>7.1</sub> O <sub>3.7</sub> N <sub>0.0</sub>	0.67	1.28	132.3	0.9	0.7	0.7	2
7	C <sub>8.9</sub> H <sub>11.4</sub> O <sub>6.3</sub> N <sub>0.0</sub>	0.72	1.28	219.0	1.4	1.5	1.9	4
8	C <sub>8.1</sub> H <sub>11.1</sub> O <sub>4.1</sub> N <sub>0.0</sub>	0.50	1.37	173.9	3.3	3.1	3.2	7
9	C <sub>4.6</sub> H <sub>5.6</sub> O <sub>3.9</sub> N <sub>0.0</sub>	0.83	1.20	123.2	3.0	3.1	5.1	6
10	C <sub>8.2</sub> H <sub>10.2</sub> O <sub>5.0</sub> N <sub>0.0</sub>	0.61	1.24	188.6	3.3	3.4	6.2	2
Unclustered					1.5	1.7	2.0	8
Filtered					15.5	17.5	20.2	206

**Table S3-2.**

Cluster #	Expt. #3 ( $\alpha$ -pinene + OH + NO) Molecular Formula	[NO]	[NO]	[NO]	[NO]	[NO]	[NO]	[NO]	[NO]	[NO]
		5 ppb	10 ppb	25 ppb	5 ppb	10 ppb	25 ppb	5 ppb	10 ppb	25 ppb
			$T_{m,50}$			$T_{m,75}$			$\Delta T$	
1	C <sub>8.8</sub> H <sub>14.3</sub> O <sub>4.7</sub> N <sub>0.0</sub>	92.4	95.7	101.9	130.0	133.1	151.1	37.6	37.4	49.2
2	C <sub>9.3</sub> H <sub>14.8</sub> O <sub>6.0</sub> N <sub>0.0</sub>	100.0	100.9	103.9	136.5	136.5	145.8	36.5	35.6	41.9
3	C <sub>7.5</sub> H <sub>10.7</sub> O <sub>6.4</sub> N <sub>0.4</sub>	101.8	97.1	101.8	145.9	142.2	146.1	44.1	45.1	44.3
4	C <sub>8.0</sub> H <sub>11.7</sub> O <sub>4.9</sub> N <sub>0.1</sub>	102.6	102.0	107.0	145.1	144.5	153.6	42.5	42.5	46.6
5	C <sub>8.0</sub> H <sub>12.0</sub> O <sub>6.0</sub> N <sub>0.0</sub>	108.4	109.4	114.0	138.0	137.3	139.3	29.6	27.9	25.3
6	C <sub>5.5</sub> H <sub>7.1</sub> O <sub>3.7</sub> N <sub>0.0</sub>	111.1	119.9	144.3	158.2	161.3	179.0	47.1	41.4	34.7
7	C <sub>8.9</sub> H <sub>11.4</sub> O <sub>6.3</sub> N <sub>0.0</sub>	122.0	119.7	125.6	156.1	152.8	159.4	34.1	33.1	33.8
8	C <sub>8.1</sub> H <sub>11.1</sub> O <sub>4.1</sub> N <sub>0.0</sub>	125.7	125.4	129.9	160.3	160.8	166.3	34.6	35.4	36.4
9	C <sub>4.6</sub> H <sub>5.6</sub> O <sub>3.9</sub> N <sub>0.0</sub>	135.9	137.4	138.9	166.4	167.1	169.3	30.5	29.7	30.4
10	C <sub>8.2</sub> H <sub>10.2</sub> O <sub>5.0</sub> N <sub>0.0</sub>	140.6	137.2	146.5	175.7	173.7	184.5	35.1	36.5	38.0
Unclustered										
Filtered										



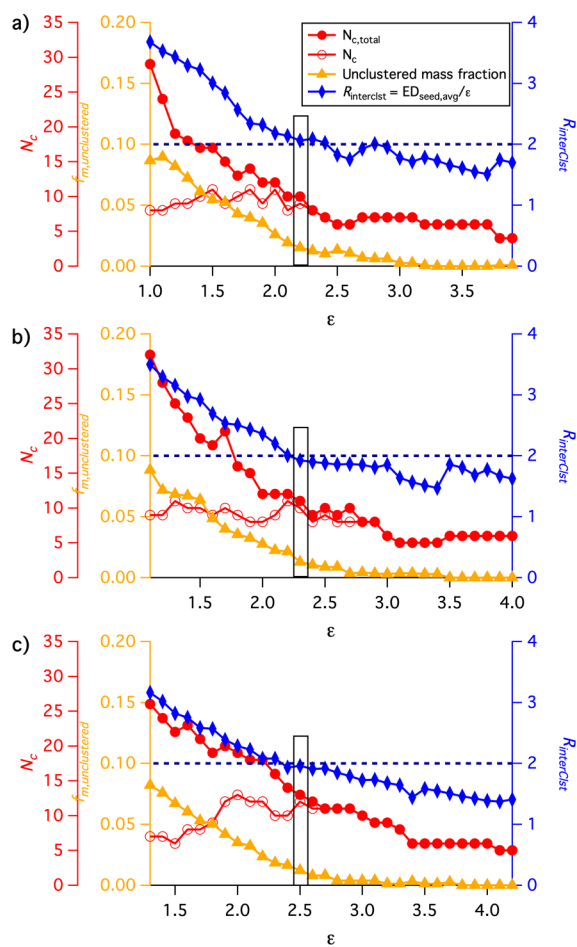


**Figure S4.** Guidance for determining the optimal  $\epsilon$  for the  $\alpha$ -pinene +OH SOA formed under (a) 5 ppb, (b) 10 ppb and (c) 25 ppb NO conditions for the multiple clustering approach. The variation of four parameters,  $N_c$ ,  $N_{c,all}$ ,  $f_{m,unclustered}$  and  $R_{interCst}$  are shown as a function of the distance criterion  $\epsilon$ . The black horizontal dashed line is guide judgement for  $R_{interCst} \geq 2$ . The values highlighted by a rectangle are the values corresponding to the optimal  $\epsilon$  used for the following clustering analysis.

**Table S4** Chemical characteristics of each cluster identified in the  $\alpha$ -pinene + OH + NO SOA system for three different NO conditions (5, 10 and 25 ppb) from the multiple-clustering approach.

**Table S4-1.** Results for the 5 ppb NO experiment.

Cluster #	Expt. #3a ( $\alpha$ -pinene+ OH+5 ppb NO)							
	Molecular Formula	O:C	H:C	Mass %	# Ions	$T_{m,50}$	$T_{m,75}$	$\Delta T$
1	C <sub>8.8</sub> H <sub>14.3</sub> O <sub>4.7</sub> N <sub>0.0</sub>	0.53	1.62	29.9	27	92.4	130.0	37.6
2	C <sub>9.3</sub> H <sub>14.8</sub> O <sub>6.0</sub> N <sub>0.0</sub>	0.65	1.59	25.4	19	100.0	136.5	36.5
3	C <sub>7.5</sub> H <sub>10.7</sub> O <sub>6.4</sub> N <sub>0.4</sub>	0.85	1.42	1.2	2	101.8	145.9	44.1
4	C <sub>8.0</sub> H <sub>11.7</sub> O <sub>4.9</sub> N <sub>0.1</sub>	0.61	1.47	12.4	10	102.6	145.1	42.5
5	C <sub>8.0</sub> H <sub>12.0</sub> O <sub>6.0</sub> N <sub>0.0</sub>	0.75	1.50	2.2	1	108.4	138.0	29.6
6	C <sub>5.5</sub> H <sub>7.1</sub> O <sub>3.7</sub> N <sub>0.0</sub>	0.68	1.28	0.9	2	111.1	158.2	47.1
7	C <sub>8.9</sub> H <sub>11.4</sub> O <sub>6.3</sub> N <sub>0.0</sub>	0.72	1.28	1.4	4	122.0	156.1	34.1
8	C <sub>8.1</sub> H <sub>11.1</sub> O <sub>4.1</sub> N <sub>0.0</sub>	0.50	1.37	3.3	7	125.7	160.3	34.6
9	C <sub>4.6</sub> H <sub>5.6</sub> O <sub>3.9</sub> N <sub>0.0</sub>	0.83	1.20	3.0	6	135.9	166.4	30.5
10	C <sub>8.2</sub> H <sub>10.2</sub> O <sub>5.0</sub> N <sub>0.0</sub>	0.61	1.24	3.3	2	140.6	175.7	35.1
Unclustered				1.5	8			
Filtered				15.5	208			

**Table S4-2.** Results for the 10 ppb NO experiment.

Cluster #	Expt. #3b ( $\alpha$ -pinene+ OH+10 ppb NO)							
	Molecular Formula	O:C	H:C	Mass %	# Ions	$T_{m,50}$	$T_{m,75}$	$\Delta T$
1	C <sub>8.5</sub> H <sub>13.6</sub> O <sub>4.9</sub> N <sub>0.1</sub>	0.58	1.60	27.6	28	95.1	134.1	39.0
2	C <sub>9.1</sub> H <sub>14.3</sub> O <sub>6.1</sub> N <sub>0.1</sub>	0.66	1.57	25.7	21	101.9	136.5	34.6
3	C <sub>8.5</sub> H <sub>12.8</sub> O <sub>4.9</sub> N <sub>0.1</sub>	0.58	1.50	17.3	14	102.1	143.3	41.2
4	C <sub>5.4</sub> H <sub>11.1</sub> O <sub>7.6</sub> N <sub>0.2</sub>	1.40	2.06	2.1	4	104.1	148.4	44.3
5	C <sub>6.8</sub> H <sub>8.4</sub> O <sub>4.6</sub> N <sub>0.0</sub>	0.68	1.23	3.2	5	110.9	159.5	48.6
6	C <sub>12.5</sub> H <sub>18.9</sub> O <sub>7.5</sub> N <sub>0.0</sub>	0.60	1.52	0.2	2	124.5	152.9	28.4
7	C <sub>9.7</sub> H <sub>14.3</sub> O <sub>7.3</sub> N <sub>0.0</sub>	0.75	1.47	0.3	2	126.5	159.3	32.8
8	C <sub>8.2</sub> H <sub>11.0</sub> O <sub>4.2</sub> N <sub>0.0</sub>	0.51	1.35	3.1	7	126.3	161.1	34.8
9	C <sub>4.0</sub> H <sub>4.0</sub> O <sub>6.0</sub> N <sub>0.0</sub>	1.50	1.00	0.5	1	134.3	168.5	34.2
10	C <sub>7.8</sub> H <sub>9.5</sub> O <sub>4.8</sub> N <sub>0.0</sub>	0.61	1.23	4.1	2	137.8	172.4	34.6
11	C <sub>3.2</sub> H <sub>3.8</sub> O <sub>3.9</sub> N <sub>0.0</sub>	1.25	1.22	1.9	4	138.6	166.3	27.7
Unclustered				1.3	10			
Filtered				12.6	195			

**Table S4-3.** Results for the 25 ppb NO experiment.

Cluster #	Expt. #3c ( $\alpha$ -pinene+ OH+25 ppb NO)							
	Molecular Formula	O:C	H:C	Mass %	# Ions	$T_{m,50}$	$T_{m,75}$	$\Delta T$
1	C <sub>10.0</sub> H <sub>15.0</sub> O <sub>6.0</sub> N <sub>1.0</sub>	0.60	1.50	1.1	1	92.3	139.8	47.5
2	C <sub>6.0</sub> H <sub>8.8</sub> O <sub>5.0</sub> N <sub>0.0</sub>	0.82	1.46	0.8	4	98.5	147.8	49.3
3	C <sub>8.1</sub> H <sub>12.4</sub> O <sub>5.4</sub> N <sub>0.2</sub>	0.66	1.53	39.8	29	103.4	150.7	47.3
4	C <sub>9.1</sub> H <sub>14.1</sub> O <sub>6.3</sub> N <sub>0.1</sub>	0.69	1.55	13.7	18	106.5	144.4	37.9
5	C <sub>6.1</sub> H <sub>9.8</sub> O <sub>6.3</sub> N <sub>0.0</sub>	1.03	1.60	3.7	2	121.2	160.9	39.7
6	C <sub>8.7</sub> H <sub>11.3</sub> O <sub>6.2</sub> N <sub>0.0</sub>	0.72	1.30	3.2	5	122.2	155.0	32.8
7	C <sub>7.9</sub> H <sub>10.7</sub> O <sub>4.8</sub> N <sub>0.1</sub>	0.61	1.36	2.8	8	125.1	165.1	40.0
8	C <sub>4.0</sub> H <sub>5.6</sub> O <sub>3.9</sub> N <sub>0.0</sub>	0.97	1.37	1.7	5	134.9	168.6	33.7
9	C <sub>11.8</sub> H <sub>18.5</sub> O <sub>7.7</sub> N <sub>0.0</sub>	0.65	1.57	0.2	3	136.5	166.2	29.7
10	C <sub>2.5</sub> H <sub>3.0</sub> O <sub>4.0</sub> N <sub>0.0</sub>	1.58	1.20	2.3	3	139.2	168.7	29.5
11	C <sub>5.2</sub> H <sub>5.8</sub> O <sub>5.1</sub> N <sub>0.0</sub>	0.97	1.11	3.8	3	140.2	175.5	35.3
12	C <sub>7.8</sub> H <sub>9.7</sub> O <sub>4.9</sub> N <sub>0.0</sub>	0.63	1.25	1.0	2	147.7	185.4	37.7
13	C <sub>4.2</sub> H <sub>4.0</sub> O <sub>3.8</sub> N <sub>0.0</sub>	0.92	0.96	1.5	2	167.5	188.9	21.4
Unclustered				0.7	7			
Filtered				16.0	205			

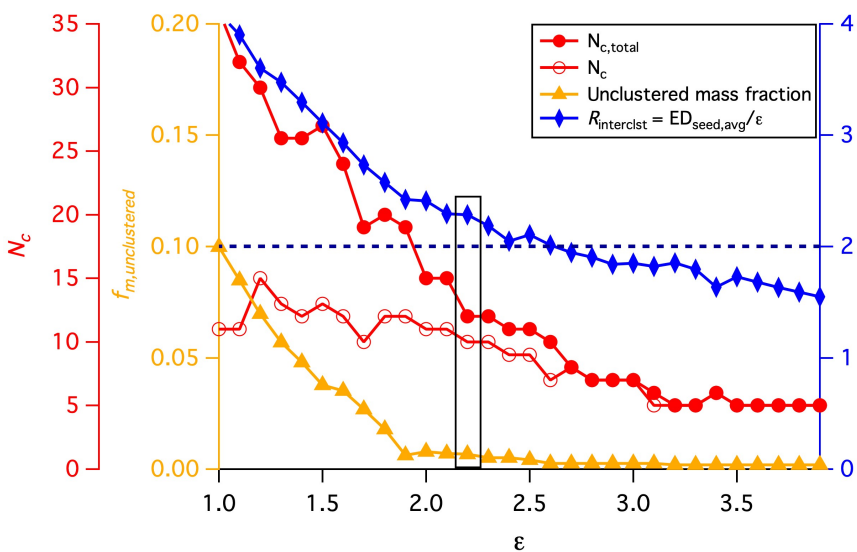


**Figure S5.** Guidance for determining the optimal  $\epsilon$  for the  $\alpha$ -pinene +O<sub>3</sub> SOA system with no isothermal evaporation for the single clustering approach. The variation of four parameters,  $N_c$ ,  $N_{c,total}$ ,  $f_{m,unclustered}$  and  $R_{interClst}$  are shown as a function of the distance criterion  $\epsilon$ . The black horizontal dashed line is guide judgement for  $R_{interClst} \geq 2$ . The values highlighted by a rectangle are the values corresponding to the optimal  $\epsilon$  used for the following clustering analysis.

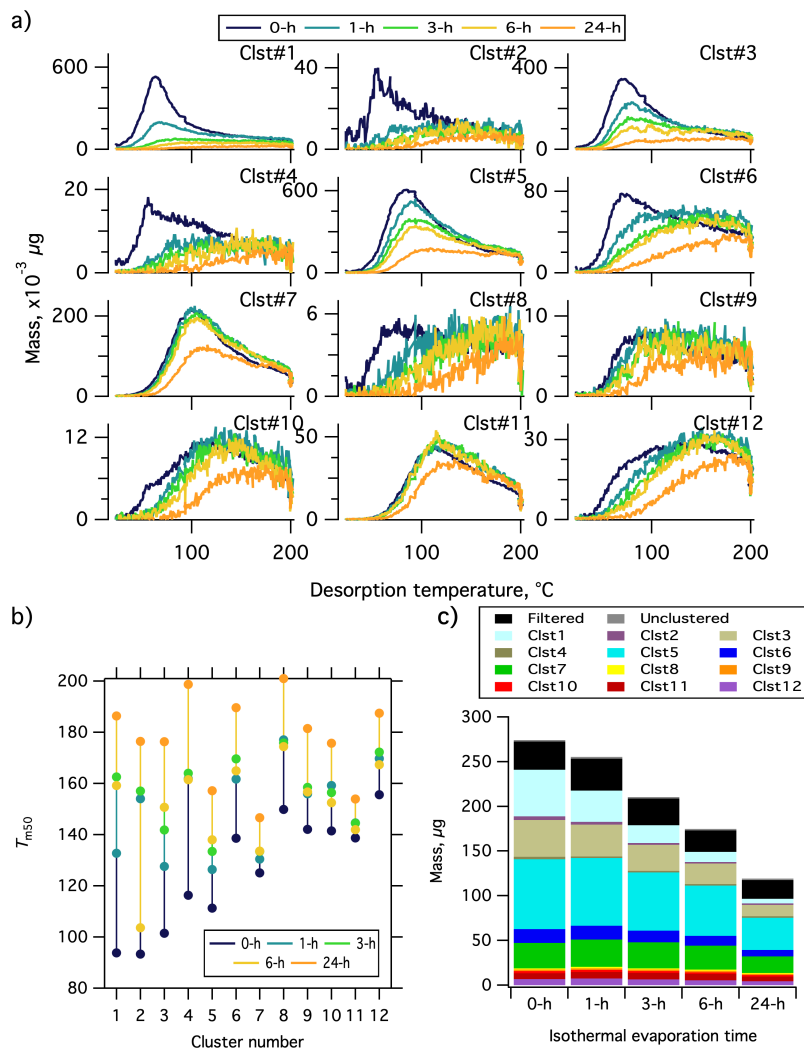


**Figure S6** Similar to **Figure 12** but presented in the absolute sense. (a) Comparison of the summed thermograms of the 12 clusters of 0-h wait (navy), 1-h wait (blue), 3-h wait (green), 6-h wait (yellow) and 24-h wait (orange) experiments. (b) Changes in the  $T_{m50}$  for all the clusters calculated from the summed thermograms, with the same color scheme as (a). (c) Absolute mass of each cluster for each experiment, including the summed mass of filtered out ions (black) and unclustered ions (gray).

**Table S5** Chemical characteristics of each cluster identified in the  $\alpha$ -pinene + O<sub>3</sub> + Evaporation SOA system from the single-clustering approach, using the no-wait experiment as the reference.

**Table S5-1.**

Cluster #	Expt. #4 ( $\alpha$ -pinene+ O <sub>3</sub> +Evap.) Molecular Formula	O:C	H:C	MW	0 h	1 h	3 h	6 h	24 h	# Ions
1	C <sub>9,8</sub> H <sub>14,0</sub> O <sub>5,7</sub> N <sub>0,0</sub>	0.58	1.42	222.8	19.0	13.7	9.5	7.0	4.8	2
2	C <sub>9,0</sub> H <sub>16,0</sub> O <sub>3,0</sub> N <sub>0,0</sub>	0.33	1.78	172.0	1.5	1.1	0.9	0.3	1.0	1
3	C <sub>8,7</sub> H <sub>14,1</sub> O <sub>4,8</sub> N <sub>0,0</sub>	0.54	1.61	195.3	15.0	14.0	14.0	13.5	11.3	9
4	C <sub>6,5</sub> H <sub>11,1</sub> O <sub>4,0</sub> N <sub>0,0</sub>	0.61	1.69	153.1	1.0	0.7	0.7	0.7	0.8	2
5	C <sub>8,9</sub> H <sub>14,0</sub> O <sub>6,1</sub> N <sub>0,0</sub>	0.69	1.58	218.4	28.5	29.6	31.0	32.1	30.3	35
6	C <sub>8,7</sub> H <sub>12,2</sub> O <sub>4,9</sub> N <sub>0,0</sub>	0.56	1.40	195.0	5.6	6.1	6.2	6.3	6.2	8
7	C <sub>12,6</sub> H <sub>23,5</sub> O <sub>7,8</sub> N <sub>0,0</sub>	0.62	1.86	299.5	10.4	12.1	14.1	15.8	16.4	34
8	C <sub>6,0</sub> H <sub>8,0</sub> O <sub>4,0</sub> N <sub>0,0</sub>	0.67	1.33	144.0	0.46	0.5	0.4	0.5	0.6	1
9	C <sub>6,7</sub> H <sub>13,9</sub> O <sub>8,2</sub> N <sub>0,0</sub>	1.22	2.07	225.5	0.6	0.7	0.7	0.8	0.9	3
10	C <sub>5,1</sub> H <sub>8,1</sub> O <sub>3,0</sub> N <sub>0,0</sub>	0.59	1.60	117.3	0.8	1.0	1.0	0.9	1.0	4
11	C <sub>13,7</sub> H <sub>24,7</sub> O <sub>8,5</sub> N <sub>0,0</sub>	0.62	1.80	325.1	2.4	2.8	3.4	4.0	4.6	8
12	C <sub>8,1</sub> H <sub>10,8</sub> O <sub>4,1</sub> N <sub>0,0</sub>	0.50	1.34	173.6	2.5	2.9	3.1	3.2	3.6	5
Unclustered					0.7	0.8	0.8	0.8	0.8	5
Filtered					11.5	14.0	14.0	13.8	17.6	185

**Table S5-2**

Cluster #	Expt. #4 ( $\alpha$ -pinene+ O <sub>3</sub> +Evap.) Molecular Formula	0 h	1 h	3 h	6 h	24 h	0 h	1 h	3 h	6 h	24 h
				$T_{m,50}$					$\Delta T$		
1	C <sub>9,8</sub> H <sub>14,0</sub> O <sub>5,7</sub> N <sub>0,0</sub>	79.6	104.3	124.4	130.6	146.4	40.1	45.9	38.3	33.4	30.1
2	C <sub>9,0</sub> H <sub>16,0</sub> O <sub>3,0</sub> N <sub>0,0</sub>	87.5	128.1	134.3	130.2	151.7	43.2	35.6	30.3	23.8	24.6
3	C <sub>8,7</sub> H <sub>14,1</sub> O <sub>4,8</sub> N <sub>0,0</sub>	93.9	107.7	117.8	126.9	141.7	33.7	40.6	38.6	34.6	32.0
4	C <sub>6,5</sub> H <sub>11,1</sub> O <sub>4,0</sub> N <sub>0,0</sub>	99.6	128.1	136.5	145.6	161.7	40.9	36.7	31.6	25.4	21.9
5	C <sub>8,9</sub> H <sub>14,0</sub> O <sub>6,1</sub> N <sub>0,0</sub>	101.0	111.5	118.3	120.6	135.0	32.5	34.5	35.8	35.4	32.6
6	C <sub>8,7</sub> H <sub>12,2</sub> O <sub>4,9</sub> N <sub>0,0</sub>	111.6	131.7	140.8	141.8	156.0	42.2	33.4	29.2	28.7	25.3
7	C <sub>12,6</sub> H <sub>23,5</sub> O <sub>7,8</sub> N <sub>0,0</sub>	114.6	120.0	122.1	123.3	131.6	32.0	32.0	31.7	32.4	30.5
8	C <sub>6,0</sub> H <sub>8,0</sub> O <sub>4,0</sub> N <sub>0,0</sub>	116.7	140.5	148.3	153.0	166.4	40.9	32.6	27.4	23.3	19.5
9	C <sub>6,7</sub> H <sub>13,9</sub> O <sub>8,2</sub> N <sub>0,0</sub>	118.6	129.0	135.7	132.6	148.5	37.6	34.3	28.8	32.0	30.4
10	C <sub>5,1</sub> H <sub>8,1</sub> O <sub>3,0</sub> N <sub>0,0</sub>	126.8	138.5	138.0	141.4	155.5	31.4	28.0	28.3	23.3	21.1
11	C <sub>13,7</sub> H <sub>24,7</sub> O <sub>8,5</sub> N <sub>0,0</sub>	127.4	131.6	133.0	131.2	140.2	29.0	29.0	28.0	27.8	26.4
12	C <sub>8,1</sub> H <sub>10,8</sub> O <sub>4,1</sub> N <sub>0,0</sub>	130.5	141.9	146.4	148.3	158.4	33.0	29.7	27.4	25.1	23.2
Unclustered											
Filtered											

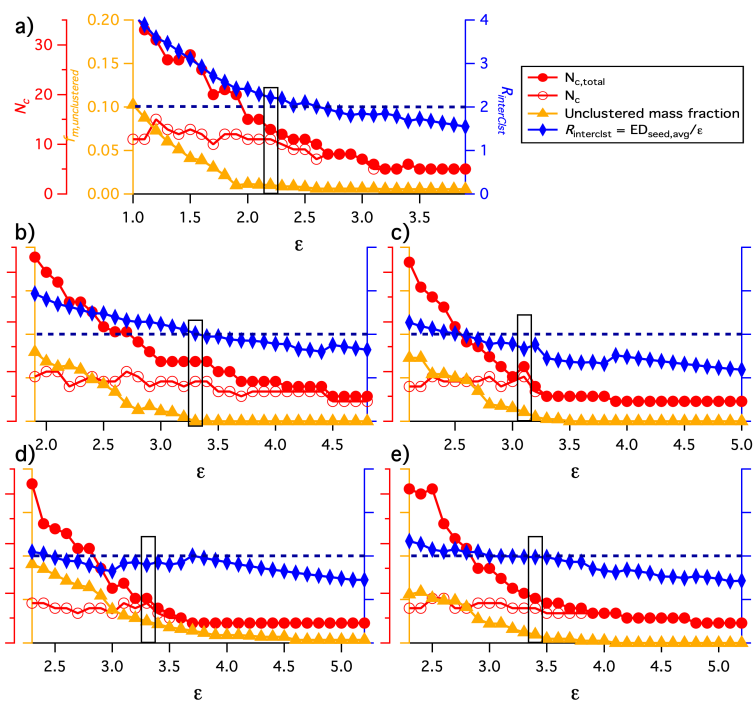


**Figure S7.** Guidance for determining the optimal  $\epsilon$  for the  $\alpha$ -pinene +  $O_3$  SOA system with (a) no isothermal evaporation (b) 1 hr (c) 3 hrs (d) 6 hrs and (e) 24 hrs of isothermal evaporation for the multiple clustering approach. The variation of four parameters,  $N_c$ ,  $N_{c,total}$ ,  $f_{m,unclustered}$  and  $R_{interClist}$  are shown as a function of the distance criterion  $\epsilon$ . The black horizontal dashed line is guide judgement for  $R_{interClist} \geq 2$ . The values highlighted by a rectangle are the values corresponding to the optimal  $\epsilon$  used for the following clustering analysis.

**Table S6** Chemical characteristics of each cluster identified in the  $\alpha$ -pinene + O<sub>3</sub> + Evaporation SOA system for five different isothermal evaporation conditions. The multiple clustering approach is used so each evaporation experiment is clustered independently.

**Table S6-1.** Results for the 0 h isothermal evaporation experiment.

Cluster #	Expt. #4a ( $\alpha$ -pinene+ O <sub>3</sub> + 0-h Evap.)							
	Molecular Formula	O:C	H:C	Mass %	# Ions	T <sub>m,50</sub>	T <sub>m,75</sub>	$\Delta T$
1	C <sub>9,8</sub> H <sub>14,0</sub> O <sub>5,7</sub> N <sub>0,0</sub>	0.58	1.42	18.9	2	79.6	119.7	40.1
2	C <sub>9,0</sub> H <sub>16,0</sub> O <sub>3,0</sub> N <sub>0,0</sub>	0.33	1.78	1.4	1	87.5	130.8	43.3
3	C <sub>8,5</sub> H <sub>13,6</sub> O <sub>4,9</sub> N <sub>0,0</sub>	0.58	1.61	12.2	8	93.6	124.3	30.7
4	C <sub>10,9</sub> H <sub>18,5</sub> O <sub>3,7</sub> N <sub>0,0</sub>	0.34	1.69	3.2	2	97.5	140.7	43.2
5	C <sub>6,5</sub> H <sub>11,1</sub> O <sub>4,0</sub> N <sub>0,0</sub>	0.61	1.69	1.0	2	99.6	140.5	40.9
6	C <sub>8,9</sub> H <sub>14,0</sub> O <sub>6,1</sub> N <sub>0,0</sub>	0.69	1.58	28.2	35	101.0	133.5	32.5
7	C <sub>8,7</sub> H <sub>12,2</sub> O <sub>4,9</sub> N <sub>0,0</sub>	0.56	1.40	5.6	8	111.6	153.8	42.2
8	C <sub>12,6</sub> H <sub>23,5</sub> O <sub>7,8</sub> N <sub>0,0</sub>	0.62	1.86	10.3	34	114.6	146.5	31.9
9	C <sub>6,0</sub> H <sub>8,0</sub> O <sub>4,0</sub> N <sub>0,0</sub>	0.67	1.33	0.5	1	116.7	157.6	40.9
10	C <sub>6,7</sub> H <sub>13,9</sub> O <sub>8,2</sub> N <sub>0,0</sub>	1.22	2.07	0.6	3	118.6	156.2	37.6
11	C <sub>5,1</sub> H <sub>8,1</sub> O <sub>3,0</sub> N <sub>0,0</sub>	0.59	1.60	0.8	4	126.8	158.2	31.4
12	C <sub>13,7</sub> H <sub>24,7</sub> O <sub>8,5</sub> N <sub>0,0</sub>	0.62	1.80	2.3	8	127.4	156.3	28.9
13	C <sub>8,1</sub> H <sub>10,8</sub> O <sub>4,1</sub> N <sub>0,0</sub>	0.50	1.34	2.5	5	130.5	163.5	33.0
Unclustered				1.0	7			
Filtered				11.4	191			

**Table S6-2.** Results for the 1 h isothermal evaporation experiment.

Cluster #	Expt. #4b ( $\alpha$ -pinene+ O <sub>3</sub> + 1-h Evap.)							
	Molecular Formula	O:C	H:C	Mass %	# Ions	T <sub>m,50</sub>	T <sub>m,75</sub>	$\Delta T$
1	C <sub>2,0</sub> H <sub>4,0</sub> O <sub>3,0</sub> N <sub>0,0</sub>	1.50	2.00	1.3	1	85.4	131.6	46.2
2	C <sub>9,4</sub> H <sub>16,7</sub> O <sub>5,2</sub> N <sub>0,0</sub>	0.55	1.79	1.6	3	96.1	125.8	29.7
3	C <sub>9,1</sub> H <sub>13,5</sub> O <sub>5,5</sub> N <sub>0,0</sub>	0.61	1.48	20.1	6	103.3	146.5	43.2
4	C <sub>9,6</sub> H <sub>15,7</sub> O <sub>6,2</sub> N <sub>0,0</sub>	0.65	1.63	36.5	48	113.9	148.4	34.5
5	C <sub>16,0</sub> H <sub>32,0</sub> O <sub>2,0</sub> N <sub>0,0</sub>	0.12	2.00	0.9	1	118.3	181.6	63.3
6	C <sub>9,0</sub> H <sub>14,0</sub> O <sub>4,0</sub> N <sub>0,0</sub>	0.444	1.56	2.6	1	120.0	162.0	42.0
7	C <sub>14,5</sub> H <sub>28,1</sub> O <sub>8,7</sub> N <sub>0,0</sub>	0.60	1.94	4.3	10	127.1	155.5	28.4
8	C <sub>8,5</sub> H <sub>12,5</sub> O <sub>5,4</sub> N <sub>0,0</sub>	0.64	1.47	4.3	6	130.8	164.3	33.5
9	C <sub>11,1</sub> H <sub>20,9</sub> O <sub>8,9</sub> N <sub>0,0</sub>	0.80	1.88	1.4	5	132.3	161.8	29.5
10	C <sub>7,4</sub> H <sub>10,1</sub> O <sub>3,9</sub> N <sub>0,0</sub>	0.52	1.36	8.6	18	140.9	171.0	30.1
11	C <sub>7,0</sub> H <sub>8,0</sub> O <sub>4,0</sub> N <sub>0,0</sub>	0.57	1.14	0.6	1	156.8	181.4	24.6
12	C <sub>17,3</sub> H <sub>34,0</sub> O <sub>2,1</sub> N <sub>0,0</sub>	0.12	1.97	1.1	2	189.2	199.1	9.0
Unclustered				0.0	0			
Filtered				16.5	210			



**Table S6-3.** Results for the 3 h isothermal evaporation experiment.

Cluster #	Expt. #4c ( $\alpha$ -pinene+ O <sub>3</sub> + 3-h Evap.)							
	Molecular Formula	O:C	H:C	Mass %	# Ions	T <sub>m,50</sub>	T <sub>m,75</sub>	$\Delta T$
1	C <sub>10.0</sub> H <sub>18.0</sub> O <sub>5.0</sub> N <sub>0.0</sub>	0.50	1.80	0.5	1	97.9	133.4	35.5
2	C <sub>9.4</sub> H <sub>14.9</sub> O <sub>6.0</sub> N <sub>0.0</sub>	0.63	1.58	16.7	13	111.8	146.2	34.4
3	C <sub>13.1</sub> H <sub>23.8</sub> O <sub>7.5</sub> N <sub>0.0</sub>	0.57	1.81	17.7	31	121.4	153.3	31.9
4	C <sub>8.6</sub> H <sub>12.8</sub> O <sub>5.3</sub> N <sub>0.0</sub>	0.62	1.49	23.1	9	121.6	159.0	37.4
5	C <sub>15.5</sub> H <sub>26.8</sub> O <sub>5.9</sub> N <sub>0.0</sub>	0.38	1.73	0.4	2	123.1	156.6	33.5
6	C <sub>8.4</sub> H <sub>12.9</sub> O <sub>6.9</sub> N <sub>0.0</sub>	0.81	1.53	4.8	8	128.3	159.0	30.7
7	C <sub>11.1</sub> H <sub>21.9</sub> O <sub>8.8</sub> N <sub>0.0</sub>	0.79	1.97	1.5	5	133.4	162.1	28.7
8	C <sub>9.0</sub> H <sub>16.0</sub> O <sub>3.0</sub> N <sub>0.0</sub>	0.33	1.78	0.9	1	134.3	164.7	30.4
9	C <sub>7.1</sub> H <sub>12.8</sub> O <sub>5.7</sub> N <sub>0.0</sub>	0.81	1.80	4.3	3	134.9	169.3	34.4
10	C <sub>7.9</sub> H <sub>10.8</sub> O <sub>4.2</sub> N <sub>0.0</sub>	0.53	1.36	13.0	22	143.4	171.6	28.2
11	C <sub>8.3</sub> H <sub>10.6</sub> O <sub>4.0</sub> N <sub>0.0</sub>	0.48	1.28	1.7	2	156.1	181.3	25.2
Unclustered				1.1	5			
Filtered				14.3	205			

**Table S6-4.** Results for the 6 h isothermal evaporation experiment.

Cluster #	Expt. #4d ( $\alpha$ -pinene+ O <sub>3</sub> + 6-h Evap.)							
	Molecular Formula	O:C	H:C	Mass %	# Ions	T <sub>m,50</sub>	T <sub>m,75</sub>	$\Delta T$
1	C <sub>9.8</sub> H <sub>14.1</sub> O <sub>6.9</sub> N <sub>0.0</sub>	0.70	1.44	4.9	3	108.2	138.3	30.1
2	C <sub>9.3</sub> H <sub>14.8</sub> O <sub>5.1</sub> N <sub>0.0</sub>	0.55	1.59	4.5	2	119.7	157.1	37.4
3	C <sub>11.9</sub> H <sub>21.0</sub> O <sub>7.3</sub> N <sub>0.0</sub>	0.61	1.76	29.2	36	121.9	154.2	32.3
4	C <sub>8.5</sub> H <sub>13.1</sub> O <sub>5.4</sub> N <sub>0.0</sub>	0.63	1.54	24.0	13	128.8	163.3	34.5
5	C <sub>11.5</sub> H <sub>23.0</sub> O <sub>9.5</sub> N <sub>0.0</sub>	0.83	2.00	0.6	2	129.2	161.7	32.5
6	C <sub>8.1</sub> H <sub>12.7</sub> O <sub>6.6</sub> N <sub>0.0</sub>	0.82	1.58	5.5	11	132.9	164.9	32.0
7	C <sub>11.0</sub> H <sub>16.0</sub> O <sub>5.0</sub> N <sub>0.0</sub>	0.45	1.45	0.4	1	144.4	172.3	27.9
8	C <sub>7.7</sub> H <sub>10.6</sub> O <sub>4.0</sub> N <sub>0.0</sub>	0.52	1.39	15.0	25	147.2	173.0	25.8
9	C <sub>2.7</sub> H <sub>5.3</sub> O <sub>3.3</sub> N <sub>0.0</sub>	1.25	2.00	0.6	2	183.9	194.9	11.0
Unclustered				2.5	11			
Filtered				12.8	203			

**Table S6-5.** Results for the 24 h isothermal evaporation experiment.

Cluster #	Expt. #4e ( $\alpha$ -pinene+O <sub>3</sub> +24-h Evap.)							
	Molecular Formula	O:C	H:C	Mass %	# Ions	T <sub>m,50</sub>	T <sub>m,75</sub>	$\Delta T$
1	C <sub>12.1</sub> H <sub>21.2</sub> O <sub>7.2</sub> N <sub>0.0</sub>	0.60	1.75	25.4	26	130.0	161.1	31.1
2	C <sub>7.0</sub> H <sub>16.0</sub> O <sub>9.0</sub> N <sub>0.0</sub>	1.29	2.29	0.6	1	133.9	166.7	32.8
3	C <sub>11.3</sub> H <sub>17.9</sub> O <sub>6.7</sub> N <sub>0.0</sub>	0.59	1.58	1.7	4	137.7	167.7	30.0
4	C <sub>11.9</sub> H <sub>20.0</sub> O <sub>8.2</sub> N <sub>0.0</sub>	0.69	1.68	4.4	10	140.1	167.6	27.5
5	C <sub>8.9</sub> H <sub>13.8</sub> O <sub>5.5</sub> N <sub>0.0</sub>	0.62	1.54	16.1	8	140.4	171.5	31.1
6	C <sub>7.9</sub> H <sub>12.0</sub> O <sub>4.6</sub> N <sub>0.0</sub>	0.58	1.51	20.3	23	154.5	179.0	24.5
7	C <sub>5.2</sub> H <sub>7.1</sub> O <sub>3.4</sub> N <sub>0.0</sub>	0.66	1.37	12.2	17	168.0	186.3	18.3
8	C <sub>16.0</sub> H <sub>32.0</sub> O <sub>2.0</sub> N <sub>0.0</sub>	0.12	2.00	1.0	1	177.9	197.9	20.0
9	C <sub>17.5</sub> H <sub>35.0</sub> O <sub>2.1</sub> N <sub>0.0</sub>	0.12	2.00	1.2	2	198.7	199.3	0.6
Unclustered				1.0	4			
Filtered				16.1	213			

## Supplemental References

D'Ambro, E. L., Schobesberger, S., Zaveri, R. A., Shilling, J. E., Lee, B. H., Lopez-Hilfiker, F. D., Mohr, C., and Thornton, J. A.: Isothermal Evaporation of alpha-Pinene Ozonolysis SOA: Volatility, Phase State, and Oligomeric Composition, *Acs Earth Space Chem*, 2, 1058-1067, <https://doi.org/10.1021/acsearthspacechem.8b00084>, 2018.

Isaacman-VanWertz, G., Massoli, P., O'Brien, R. E., Nowak, J. B., Canagaratna, M. R., Jayne, J. T., Worsnop, D. R., Su, L., Knopf, D. A., Misztal, P. K., Arata, C., Goldstein, A. H., and Kroll, J. H.: Using advanced mass spectrometry techniques to fully characterize atmospheric organic carbon: current capabilities and remaining gaps, *Faraday Discussions*, 200, 579-598, <https://doi.org/10.1039/c7fd00021a>, 2017.

Lee, B., Lopez-Hilfiker, F. D., D'Ambro, E. L., Zhou, P. T., Boy, M., Petaja, T., Hao, L. Q., Virtanen, A., and Thornton, J. A.: Semi-volatile and highly oxygenated gaseous and particulate organic compounds observed above a boreal forest canopy, *Atmospheric Chemistry and Physics*, 18, 11547-11562, <https://doi.org/10.5194/acp-18-11547-2018>, 2018.

Lee, B. H., Lopez-Hilfiker, F. D., Mohr, C., Kurten, T., Worsnop, D. R., and Thornton, J. A.: An Iodide-Adduct High-Resolution Time-of-Flight Chemical-Ionization Mass Spectrometer: Application to Atmospheric Inorganic and Organic Compounds, *Environ Sci Technol*, 48, 6309-6317, <https://doi.org/10.1021/es500362a>, 2014.

Liu, J. M., D'Ambro, E. L., Lee, B. H., Lopez-Hilfiker, F. D., Zaveri, R. A., Rivera-Rios, J. C., Keutsch, F. N., Iyer, S., Kurten, T., Zhang, Z. F., Gold, A., Surratt, J. D., Shilling, J. E., and Thornton, J. A.: Efficient Isoprene Secondary Organic Aerosol Formation from a Non-IEPDX Pathway, *Environ Sci Technol*, 50, 9872-9880, <https://doi.org/10.1021/acs.est.6b01872>, 2016.

Liu, S., Shilling, J. E., Song, C., Hiranuma, N., Zaveri, R. A., and Russell, L. M.: Hydrolysis of Organonitrate Functional Groups in Aerosol Particles, *Aerosol Science and Technology*, 46, 1359-1369, <https://doi.org/10.1080/02786826.2012.716175>, 2012.

Lopez-Hilfiker, F. D., Mohr, C., Ehn, M., Rubach, F., Kleist, E., Wildt, J., Mentel, T. F., Lutz, A., Hallquist, M., Worsnop, D., and Thornton, J. A.: A novel method for online analysis of gas and particle composition: description and evaluation of a Filter Inlet for Gases and AEROsols (FIGAERO), *Atmospheric Measurement Techniques*, 7, 983-1001, <https://doi.org/10.5194/amt-7-983-2014>, 2014.